

1 4D porosity evolution during pressure-solution of NaCl in the presence
2 of phyllosilicates

3

4 **Alice Macente**^{a,1}, Florian Fousseis^a, Ian B. Butler^a, Erika Tudisco^b, Stephen A. Hall^c, Edward Andò^d

5 ^a University of Edinburgh, School of Geosciences, The King's Buildings, James Hutton Road,
6 Edinburgh EH9 3FE

7 ^b Lund University, Division of Geotechnical Engineering, John Ericssons väg 1, Lund, Sweden

8 ^c Lund University, Department of Solid Mechanics, Ole Römers väg 1, 223 63 Lund, Sweden

9 ^d Univ. Grenoble Alpes, CNRS, Grenoble INP², 3SR, F-38000 Grenoble, France

10 Corresponding author: Alice Macente

11 Corresponding author's email: alice.macente@gmail.com

12

This is a peer-reviewed, accepted author manuscript of the following article: Macente, A., Fousseis, F., Butler, I. B., Tudisco, E., Hall, S. A., & Andò, E. (2018). 4D porosity evolution during pressure-solution of NaCl in the presence of phyllosilicates. *Earth and Planetary Science Letters*, 502, 115-125. <https://doi.org/10.1016/j.epsl.2018.08.032>

¹ Stanford University, Department of Geophysics, 397 Panama Mall, Stanford, CA 94305

² Institute of Engineering Univ. Grenoble Alpes

13 **Abstract**

14 Pressure-solution creep is one of the most common crustal deformation mechanisms, inducing
15 changes in the porosity and permeability of rocks. For a variety of rock types undergoing pressure
16 solution, it has been shown that the presence of phyllosilicates may significantly enhance the
17 rate of the pressure-solution process. In this experimental investigation, we present 4-
18 dimensional (three dimensions + time) X-ray microtomographic data that contrast deformation
19 by pressure-solution of a pure NaCl aggregate with that of a mixture of NaCl and biotite. The
20 results show that for mixed samples (NaCl+biotite), phyllosilicates induce a marked reduction in
21 porosity and pore connectivity and contribute to an increase in the local strain rates by an order
22 of magnitude over pure NaCl samples. At the same time, phyllosilicates do not induce strain
23 localization in the sample. We discuss various possible explanations for these observations
24 including a possible positive feedback between the porosity distribution and pressure solution.
25 Our study yields novel insights into the local effects of phyllosilicates during pressure-solution
26 creep and provides full 4-dimensional imaging and characterization of the coupled evolution of
27 porosity and pore connectivity over previously unprecedented experimental time scales.

28

29 **Keywords (6):** pressure-solution creep; phyllosilicates; X-ray microtomography; Digital Volume
30 Correlation; geochemical self-organization;

31

32 **1. INTRODUCTION**

33 Pressure-solution creep (PSC) is one of the key mechanisms of fluid-rock interaction and
34 can induce significant changes in the transport properties and the composition of rocks. A wide

35 range of geoscience applications, including hydrocarbon extraction, CO₂ storage and geothermal
36 energy harvesting from hot sedimentary aquifers, rely on an accurate knowledge of the porosity
37 and permeability of reservoir rocks. Understanding how these properties are affected by PSC is
38 therefore of crucial importance.

39 PSC is a solution mass transfer process in response to the application of non-hydrostatic
40 stresses that involves (i) dissolution at stressed contact points, (ii) mass transport through a fluid
41 phase along grain boundaries, and (iii) re-precipitation of the dissolved material in the nearby
42 low-stress areas (pores, veins) (Gratier et al., 2013; Rutter, 1983). PSC induces changes in the
43 microstructure, pore structure, composition and strength of a wide range of geological materials
44 (e.g. Aharonov and Katsman, 2009; Angevine and Turcotte, 1983; Bos et al., 2000; Croizé et al.,
45 2010; Gratier, 1993; Gratier et al., 2005; Hickman and Evans, 1995, 1991; Lehner and Leroy, 2004;
46 Pluymakers and Spiers, 2015). These alterations may, in turn, affect the transport properties of
47 rocks (Sprunt and Nur, 1977, 1976). PSC has also been observed to trigger strain localization
48 leading to the formation of stylolites (Gratier, 2003; Gratier et al., 2013;). Strain localisation
49 during PSC has been recognized as involving feedbacks between solution/precipitation reactions
50 and an evolving pore structure and thus a coupling between chemical, mechanical and hydraulic
51 processes (Merino et al., 1983; Ortoleva et al., 1987).

52 While the effects of PSC on transport properties have been investigated extensively in a
53 wide range of rocks (see Gratier et al. (2013), and references therein), the dynamic evolution of
54 these coupled processes at the grain scale remains poorly understood. This is primarily caused
55 by the previously limited possibilities to image PSC in three dimensions over time. Renard et al.
56 (2004) were the first to use 4-dimensional (4D, three spatial dimensions and time) synchrotron-

57 based X-ray microtomography (μ CT) to study the effects of PSC during compaction of pure NaCl
58 aggregates. They imaged the reduced pore space and the impingement of grain contacts and
59 inferred that the mean permeability in their samples decreased dramatically during compaction.
60 Despite its pioneering character, this study did not explore PSC in the presence of phyllosilicates,
61 which have been shown to hold the potential to significantly affect the rate of PSC (Aharonov
62 and Katsman, 2009; Bos and Spiers, 2002; Hickman and Evans, 1995; Renard et al., 1997). Here
63 we present 4D X-ray microtomographic data that contrast the deformation of a pure NaCl
64 aggregate by PSC with that of a mixture of NaCl and biotite, in order to investigate the effects of
65 phyllosilicates on the progressive shortening and the concomitant evolution of porosity and pore
66 connectivity of the samples. The combination of μ CT with *Digital Volume Correlation* (DVC, e.g.
67 Andò et al., 2012; Tudisco et al., 2017) enables quantification of strain and strain rates at the
68 grain scale and following of the evolution of these parameters during sample compaction. Our
69 findings suggest that in NaCl aggregates: i) bulk porosity and pore connectivity are critically
70 reduced in the presence of phyllosilicates; ii) phyllosilicates contribute to increase the strain rates
71 achieved by PSC by an order of magnitude with respect to the monomineralic NaCl domains.

72

73 **2. MATERIAL AND METHODS**

74 **2.1 Introduction**

75 We use NaCl aggregates as analogues for geomaterials and sedimentary rocks undergoing
76 PSC. Previous compaction experiments have demonstrated that NaCl samples deform sufficiently
77 quickly to enable the study of PSC in a laboratory environment at room temperature (Gratier,
78 1993; Renard et al., 2004, 2001; Schutjens and Spiers, 1999; Spiers et al., 1990).

79 2.2 Materials

80 2.2.1 Sample Preparation

81 Two different samples were prepared in x-ray transparent uniaxial presses (see section 2.2.2)
82 to test the effect of different sample compositions on PSC. The total sample mass was chosen to
83 produce cylindrical samples with diameters of 5 mm and an initial height of ~5 mm. For the first
84 sample, granular NaCl (analytical reagent, Fisher Scientific) was sieved to a 250-300 μm grain size.
85 This sample acted as our monomineralic reference. The second sample consisted of a mixture of
86 NaCl and biotite grains at a ratio, by mass, of 4:1. The NaCl was sieved to give the same grain size
87 as the first sample. Biotite flakes with grain sizes between 212 and 750 μm (longest dimension)
88 were obtained by cutting mica sheets from a biotite single crystal using a scalpel. Biotite was
89 chosen because of the contrast in X-ray absorption with respect to NaCl; in μCT data biotite flakes
90 appears as bright grains, NaCl appears as light grey grains, while (brine-filled) pores are dark grey
91 (Fig. 1). In the press, the NaCl/biotite mixture (1.4 mm thick) was confined by two pure NaCl
92 layers (0.95 mm top layer, 1.27 mm bottom layer). In this way, the two pure NaCl layers constitute
93 a 'reference' material within the sample to compare the degree of compaction under the same
94 experimental conditions. The materials were introduced into the presses sequentially as slurries.
95 Biotite within the central layer showed no preferential alignment prior to compaction. In each of
96 the two samples, two discs of filter paper were placed above and below of the samples, to avoid
97 grains clogging the fluid connections. Both samples were saturated with NaCl solution. The initial
98 porosity of the two sample compositions has been calculated from the mass of the salt
99 quantitatively added and the dimensions of the initial salt reference stack. The pure NaCl sample
100 exhibits an initial porosity of ~36%, while the sample with biotite, due to the different grain

101 packing and an initial different height (5 mm in NaCl vs 3.7 mm in NaCl-biotite), exhibits a porosity
102 of ~33%.

103 **2.2.2. Experimental Setup**

104 The samples were compacted in X-ray transparent presses. These experimental presses were
105 built in-house and comprise a 5 mm diameter cylindrical piston that was fashioned to be a close
106 running-fit to the lower cylindrical sample chamber (Supplementary Fig. S3). The cells were
107 manufactured from PEEK (Polyether-ether-ketone). Loading frames, composed of two 20 mm
108 thick Perspex plates joined by three threaded rods, allowed a pneumatic actuator to apply a
109 constant uniaxial load on the samples. The close running-fit of the piston enabled a narrow
110 annulus of high-vacuum silicone grease to be used to provide a fluid seal between the piston and
111 sample chamber.

112 Initial loading of the sample using the pneumatic actuator for 10 minutes was used to
113 produce a pre-compacted starting material. At this stage, a reference μ CT scan was acquired (see
114 section 2.2.3). Subsequently, the inlet and outlet tubes to the cell, as well as the sample, were
115 flushed with a pre-saturated NaCl solution to ensure that no air bubbles remained in the system,
116 enabling the experiments to start saturated with brine. To maintain fluid saturation, a pre-
117 saturated NaCl solution filled reservoir attached to the lower fluid inlet of the cell was mounted
118 ~40 cm above the cells (Supplementary Fig. S3). The sample was then loaded to a constant
119 uniaxial stress which was stable between 6.4 and 6.6 MPa.

120 **2.2.3 Image Acquisition**

121 During each experiment, 3D μ CT data were acquired using the custom-built microtomograph
122 in the School of Geosciences, at the University of Edinburgh (see Cnudde and Boone (2013), for

123 the fundamentals of laboratory X-ray μ CT and Table S1 for data acquisition parameters).
 124 Combined, the data acquired during the experiments formed a 3D time series, i.e. 4D datasets.
 125 Compaction was interrupted for scanning of the samples. For each sample, twelve μ CT datasets
 126 were acquired over 2455 hours of compaction (Fig. 2, 3, Table S2), allowing monitoring of the
 127 evolution of porosity and grain morphologies over time. Initially, the samples were scanned in
 128 short time intervals (2, 4, 6 hours), to monitor the mechanical behaviour of the samples, and
 129 capture relatively rapid initial deformation. Successively, the time interval between each scan
 130 was increased to monitor the progressively slower deformation of the sample (Table S2).

131 **2.2.4 Image Processing**

132 The μ CT data were reconstructed using Octopus[®] software (Dierick et al., 2004) yielding
 133 a voxel (3-dimensional pixel) volume of $6.5^3 \mu\text{m}^3$. The twelve microtomographic volumes
 134 acquired for each deformation experiment were analysed individually, to assess sample
 135 compaction and to measure the evolution of porosity and pore connectivity. The height of the
 136 samples in between the top piston and the bottom of the cell was measured from the vertical
 137 slices through each μ CT scan, and the relative shortening was calculated through

$$138 \quad \varepsilon_t = \frac{x_0 - x_t}{x_0}$$

139 where x_0 represents the initial height of the sample (measured from the reference scans), and x_t
 140 represents the height at a given time t . The μ CT datasets were denoised using a *median filter*
 141 with a kernel size 2. Subvolumes of dimensions 400^3 voxels, equivalent to a cube of 17.6 mm^3
 142 (i.e., 2.6 mm on each side), were cropped from the central regions of the reconstructed μ CT
 143 volumes to conduct porosity analyses and avoid artefacts from the cell boundaries. The
 144 workflow, applied in AvizoFire[®] v. 8 and Avizo[®] v. 9, is detailed in Supplementary Figure S4. The

145 pore space was segmented by the application of an *interactive threshold* to produce binarised
146 image stacks from which the total porosity was determined using the *volume fraction* operator
147 (Arns et al., 2002) (Fig. 4a). The sensitivity of the segmentation and interconnectivity analysis to
148 changes in the threshold values was established by repeating the procedure on volumes that
149 were eroded and dilated by one voxel (see Fusseis et al. (2012) and Macente et al. (2017) for
150 details of the analysis). This procedure yielded error bars on the porosity measurements. Slice-
151 by-slice (2-dimensional) porosity analyses were also performed to determine the evolution of the
152 porosity along the direction of loading (Fig. 4b, c, d).

153 Pore space connectivity was characterized in the segmented data using the *label* function
154 and a voxel coordination value of six, where the *labeling* operator identifies neighbouring voxels
155 that share a cube face and assigns them to an individual pore cluster (Fig. 5, 6). From these
156 clusters, individual pores were separated using the *Separate Objects* operator with a
157 coordination number of six, and a marker extent equal to one (least connected objects).
158 Separation points represent pore throats. Subsequently, the individual pores were analysed for
159 their volume in the individual datasets using the *Label analysis* operator. The smallest pores
160 considered in the pore size distribution analyses were 10 voxels in volume, or $2.7 \times 10^3 \mu\text{m}^3$.

161 We treated the central mixed layer and the marginal pure NaCl layers in the NaCl-biotite
162 sample as three discrete subdomains in order to assess and compare their relative evolution.
163 From the 400^3 voxels subvolumes, these subdomains were extracted using the *Extract volume*
164 operator in Avizo, by identifying where the biotite flakes first occur and end vertically along the
165 sample. The marginal NaCl layers were also compared with the pure NaCl sample.

166 **2.3 Digital Volume Correlation (DVC)**

167 Digital Volume Correlation (DVC) was used to measure the local distribution of
168 displacements (from which maximum shear strains and volumetric strains are obtained) in the
169 sample between two successive time steps (see Supplementary Material for details on the
170 technique). DVC, which spatially resolves displacements with a sub-voxel accuracy, was
171 performed on consecutive pairs of μ CT 3D datasets using the code *TomoWarp2* (Tudisco et al.,
172 2017) and computed on the Edinburgh Compute and Data Facility's Terracorrrelator cluster
173 (Atkinson et al., 2015). Results were visualized in the open-source software Fiji (Schindelin et al.,
174 2012). Misalignments in x and y, and misorientation in excess of 5° between the two 3D datasets
175 can introduce errors in the outputs of the correlation and needed to be corrected. Two small
176 markers at the base of the experimental cells were used together with the central fluid bore in
177 the press to define the position and orientation of the datasets to enable the correction of
178 misalignments and misorientations between two subsequently acquired time steps using the
179 *rotate* and *translate* operators in Fiji. Figures 7 and 8 show the 3-dimensional results of DVC
180 represented by XZ vertical slices through the middle of the analysis volumes for progressively
181 shortened datasets. Absolute strain-rate values were calculated by dividing the DVC strains by
182 the duration of loading (in seconds) between each analysed μ CT scan (Fig. 9).

183 **2.4 Scanning electron microscopy**

184 Secondary electron images were acquired after the deformation experiments to study the
185 grain-scale effects of pressure solution in the sample. Before retrieving the samples, the brine
186 was displaced using compressed air. The samples were then retrieved from the uniaxial cells and
187 portions of the samples carefully extracted. This procedure may introduce physical damage to
188 the sample microstructures. For this reason, we only investigated evidence for PSC (i.e. indented

189 grains, suture zones) in areas that were ‘undisturbed’ and represented consolidated portions of
190 the original samples. Gold coated samples were imaged using a Carl Zeiss SIGMA HD VP Field
191 Emission SEM with an acceleration voltage of 10 kV. Samples were mounted on an aluminium
192 stub using a self-adhesive conducting pad prior to gold coating.

193 **3. RESULTS**

194 **3.1 Bulk deformation**

195 The measurements of vertical shortening show that the *pure NaCl* sample shortened a
196 total of 25 % over 2455 hours of compaction. The compaction curve was initially steep, where
197 the sample accommodated 10 % vertical shortening in 22.5 hours. Between 155 and 255 hours,
198 the compaction rate slowed down. Beyond 400 hours of compaction, the gradient of the curve
199 did not change substantially and we consider the sample to deform in steady state there (Fig.
200 2a). The compaction curve for the *NaCl-biotite* sample displays an identical pattern. However,
201 the sample reached a total of 35 % vertical shortening at the end of the experiment, with very
202 fast shortening of ~17 % in the first 22.5 hours. Compaction decelerated over the same time
203 interval as the pure NaCl sample, again reaching what appears to be a steady state deformation.
204 In both experiments, compaction was still ongoing at the end of the experiment.

205 These trends are reflected by the evolution of bulk strain rates over time (Fig. 2b). The
206 data showed an immediate decrease in bulk strain rates after initial compaction. Some
207 differences were present between 208 and 376 hours of compaction, when the two samples
208 deformed less over a significant time period, resulting in lower strain rates (Fig. 2b).

209 Inspection of vertically centred slices through the μ CT data revealed some key differences
210 between the two samples (Fig. 3). The NaCl sample showed no microstructures indicative of the

211 action of cataclasis, nor indented grains to have formed in the first 100 hours. However, after
212 some compaction, porosity was reduced and grains started to agglomerate (Fig. 3c, d). In the
213 NaCl-biotite sample, the porosity reduction was localised in the biotite-bearing layer early on
214 (Fig. 3f). In this layer, NaCl grains lost their cubic habit with increasing compaction. Biotite
215 generally showed a progressive alignment in the direction perpendicular to the loading, although
216 some grains were trapped in their orientation and left without room to move (Fig. 3 e-h, centre
217 bottom). In comparison, the marginal NaCl layers developed fewer NaCl grain impingements, and
218 ~10 % of porosity remained after 2455 hours of compaction. These observations mirrored those
219 from the pure NaCl sample.

220

221 **3.2 Porosity evolution**

222 **3.2.1 Bulk Porosity**

223 We analyzed the distribution of porosity change during compaction in the cropped
224 subvolumes to identify any heterogeneities that could be indicative of strain localization in our
225 samples and to evaluate the evolving transport properties (Fig. 4a). In the case of the pure NaCl
226 sample, as compaction proceeded the bulk porosity was reduced from 36 to ~13 % (Fig. 4a).
227 Slice-by-slice porosity measurements along the vertical axis of the sample (Z-direction) confirm
228 that this porosity reduction was evenly distributed in the sample and that no strain localization
229 had taken place (Fig. 4b, c, d). The upper portion of the sample showed a slightly larger decrease
230 in porosity as compared to the rest of the sample. In the case of NaCl-biotite sample, bulk porosity
231 decreased by ~25 % over the duration of the experiment (Fig. 4a). The slice-by-slice analysis

232 shows that at some vertical positions porosity decreased to 0 % after 2465 hours of compaction
233 (Fig. 4d).

234 To better illustrate the effect of sample composition, shortening was evaluated separately
235 for the biotite-bearing layer and the marginal NaCl layers of this sample (Fig. 5). The marginal
236 NaCl-bearing layers were combined in the analysis. Essentially, shortening was accommodated
237 to roughly equal parts by all three layers. The biotite-bearing layer shortened marginally more
238 (36 %), with its thickness decreasing from 1.4 mm to 0.9 mm over 2455 hours (Fig. 5). In the same
239 time interval, the NaCl layers shorten from 2.2 mm to 1.5 mm in total (35 % shortening). This
240 analysis also reveals how shortening was partitioned between the three layers (Fig. 5). Initially,
241 both layers compacted at about the same rate. At 91 hours, the shortening was partitioned into
242 the marginal NaCl layers, a development that continued to 376 hours. At 137.5 hours the pore
243 connectivity in the biotite-bearing layer broke down (see section 3.2.2 below), as shown by the
244 grey shaded area in Fig. 5. This event was followed by accelerated compaction in the biotite-
245 bearing layer and a deceleration of compaction in the NaCl layers. From 376 hours onwards, both
246 layers compacted at about the same rate, until the end of the experiment.

247

248 We further analysed the pore size distribution in the two sample compositions
249 (Supplementary Fig. S5) for three compaction steps (beginning, middle and end of the
250 compaction). In both samples, the absolute frequency of larger volume pores decreased and that
251 of smaller pores increased with increasing compaction. In the NaCl sample, small pores (volume
252 $< 2.6 \times 10^5 \mu\text{m}^3$) doubled in frequency with increasing deformation. However, these pores
253 contributed relatively small amounts to the total pore volume (Supplementary Fig. S5c). Similar

254 observations were made in the NaCl-biotite sample. To better understand the effect of the
255 central biotite-bearing layer, we analysed the pore size distributions in this layer and the marginal
256 NaCl layers in five increasingly shortened datasets (Supplementary Fig. S6). The pore size
257 distribution for the marginal NaCl layers showed a general increase in smaller pore sizes (volumes
258 $< 2.6 \times 10^5 \mu\text{m}^3$) and a corresponding decrease in the number of larger pores, which resembled
259 the evolution of the pure NaCl sample (Supplementary Fig. S6a). However, the central biotite-
260 bearing layer showed a much more marked reduction for large pores (Supplementary Fig. S6b).

261

262 **3.2.2. Pore Connectivity**

263 We further analysed how compaction affected pore connectivity via pore throats (as
264 opposed to grain boundaries, which we could not resolve in our data) in the two samples. The
265 homogeneity of the pure NaCl sample is assumed to be responsible for the preservation of a
266 percolating pore network throughout the sample until the end of the experiment (Fig. 6). The
267 largest connected pore cluster (volume $> 2.7 \times 10^8 \mu\text{m}^3$) initially accounted for all the pore space;
268 however, in later compaction stages ~ 3 % of the porosity was accommodated by smaller, isolated
269 pores (Fig. 6 top). In contrast, the NaCl-biotite sample was characterized by a marked difference
270 in the evolution of pore connectivity in the central NaCl-biotite layer and the marginal NaCl layers
271 (Fig. 6 bottom). While the pore space was initially connected throughout the entire sample, with
272 99.8 % of the segmented porosity being accommodated by a single pore cluster, porosity started
273 to disconnect vertically across the NaCl-biotite layer after 137.5 hours of compaction. Eventually
274 two large pore clusters, disconnected from each other, remained present at the top and bottom
275 of the sample, in total constituting 88 % of the total pore space (Fig. 6). A significant proportion

276 of porosity was accommodated by smaller, isolated pores, mostly located at the interfaces with
277 the marginal NaCl layers (not shown in Fig. 6).

278 **3.3 Local strains and strain rates: results from DVC analysis**

279 DVC was applied to every successive pair of compaction steps, yielding the evolving
280 displacement fields during the entire experiment using eleven DVC datasets per sample. The DVC
281 analysis of the pure NaCl sample showed a relatively homogeneous distribution of shear strains,
282 with local maxima (Fig. 7, Supplementary Gif1). These zones correspond to zones where the
283 volumetric strain is negative, indicating compaction (white circles in Fig. 7).

284 In comparison, the DVC analysis of the NaCl-biotite sample showed a much more
285 heterogeneous shear strain distribution at the beginning and again at the end of the experiment,
286 with a concentration of shear strains in the NaCl-biotite layer (Fig. 8, Supplementary Gif2). The
287 analyses of volumetric strains in this sample showed a concentration of compaction in the centre
288 of the sample (white circles in Fig. 8), with the highest strains being accumulated in the early and
289 late stages of the experiment.

290 Calculating the local integrated strain rates from DVC analyses enabled contrasting the
291 bulk compaction rate of each sample with locally resolved strain rates on the grain scale (Fig. 9).
292 While in both samples the bulk compaction rates decreased by two orders of magnitude during
293 the duration of the experiment (10^{-6} to 10^{-8} s^{-1} , Fig.2), locally (i.e. on the grain scale) both samples
294 showed significant deviations in strain rates (Fig. 2). In the pure NaCl sample, the local shear
295 strain rates decreased from 10^{-6} – 10^{-7} to 10^{-8} – 10^{-9} s^{-1} , whereas volumetric strain rates decreased
296 from -10^{-6} to -10^{-8} s^{-1} in the most compacted areas. However, these values were evenly distributed
297 within the sample (Fig. 9). In contrast, the shear strain rates reached maximum values of 10^{-7} s^{-1}

298 in the presence of biotite, while the highest volumetric compaction rates were $-6 \times 10^{-8} \text{ s}^{-1}$. The
299 high shear- and lower volumetric strain rates occur in the central NaCl-biotite layers (Fig. 9) and
300 are an order of magnitude higher than in the rest of the sample.

301 **3.4 Microstructural evidence for PSC**

302 SEM images of the recovered samples were acquired in order to verify the microstructural
303 changes and to collect evidence for PSC, if present, on the grain scale (Fig. 10). Indented contacts
304 would provide evidence for PSC consistent with that proposed by Passchier and Trouw (2005)
305 (page 31, box 3.2). In the pure NaCl sample, grains that have lost their original cubic habits are
306 clearly visible (Fig. 10a, b). In some areas, it is possible to recognize triple junctions (Fig. 10a) and
307 suture zones between grain interfaces, where the two grain contacts are highly indented (Fig.
308 10b). In the presence of phyllosilicates, indentations are obvious and NaCl grains can be seen that
309 have dissolved against (less soluble) biotite grains, and NaCl grains that have lost their cubic habit
310 and have become more rounded are also evident (Fig. 10c, d). In the pure NaCl portions of this
311 sample, indentations between NaCl grains can still be observed, but the grains have retained
312 more of their original habit (Fig. 3).

313 **4. DISCUSSION**

314 **4.1 Bulk and local deformation evolution**

315 Our experiments enable a direct comparison of bulk compaction behaviour with local
316 grain-scale responses and thus allow novel insights into the effects of sample composition on the
317 deformation processes. The bulk compaction curves of the two investigated sample
318 configurations (Fig. 2a) show a strong non-linear decrease in the compaction rate over time,
319 which is in agreement with findings from previous studies and support our conclusion that NaCl

320 deforms by PSC (Hickman and Evans, 1995, 1991; Renard et al., 2004; Schutjens and Spiers, 1999;
321 Spiers et al., 1990). However, the duration of our experiments considerably exceeded that of
322 many published studies (Renard et al., 2004; Rutter and Wanten, 2000; Spiers et al., 1990;), which
323 allows a more detailed assessment of the evolution of compaction behaviour of halite samples.
324 Earlier, shorter studies by Renard et al. (2004) and Spiers et al. (1990) showed a very similar
325 compaction behaviour despite slightly different experimental setups. Renard et al. (2004) used a
326 smaller grain size of sieved NaCl (100-150 μm), and smaller loads (0.1 to 0.6 MPa) and conducted
327 their experiment at room temperature for seven days. The compaction rate decreased over time,
328 showing an initial steep gradient, as in our data, and reaching 18 % of vertical shortening after
329 three days. They concluded that the presence of clays supports grain contact healing, reducing
330 porosity and favouring pressure-solution creep. Spiers et al. (1990) performed tests on brine-
331 saturated NaCl powder (grain size 100-275 μm) at temperatures of 20-90°C and applied stresses
332 of 0.5-2.2 MPa, testing theoretically-derived constitutive equations. Their grain sizes and time
333 intervals are similar to ours, and their results showed similar orders of bulk strain rates. The data
334 presented here explore the time evolution beyond the initial steep compaction rate shown in
335 these studies and provide a visual assessment of the micro-scale processes, feeding into a better
336 understanding of the role of phyllosilicates.

337 The striking observation from our own experiments is that both samples follow essentially
338 the same bulk compaction path, with a very rapid initial compaction characterized by variable
339 rates (Fig. 2 a, b), replaced by what appears to be steady state compaction after about 400 hours.
340 We interpret mechanical grain rearrangements and accelerated dissolution rates at initially
341 relatively small and, therefore, highly stressed grain contact areas to be responsible for the high

342 compaction rates during the early stages of the experiments. The decrease in the compaction
343 rate up to about 400 hours might broadly reflect an increase in grain contact area and the
344 associated decrease in local normal stresses as drivers for dissolution.

345 From about 400 hours until the end of the experiments at 2455 hours, both experiments
346 compacted by PSC at virtually the same constant rates (Fig. 2b), which raises questions about the
347 actual effect of biotite upon PSC in the NaCl-biotite sample. In our interpretation, we consider it
348 of importance that, while the local shear strain rates reached up to $3 \times 10^{-8} \text{ s}^{-1}$ in the pure NaCl
349 sample, these maxima tended to be transient in terms of their location and moved throughout
350 the sample (cf. Fig. 9a). We interpret this as the capture of dynamic rearrangements of stresses
351 in the compacting sample (see below). The NaCl-biotite sample showed similar magnitudes of
352 local strain rates, but in that case, these were clearly associated with the loci of biotite flakes and
353 remained so over the entire duration of the experiment (Fig. 8, 9). We further observe that the
354 presence of biotite was clearly related to the reduction of porosity (Fig. 4 b-d), which, in the
355 absence of strain localization in the central NaCl-biotite layer (Fig. 5), cannot be ascribed to pore
356 collapse there and rather points to pores having been filled.

357
358 On the basis of these observations, we interpret PSC in the NaCl and NaCl-biotite layers,
359 to have operated under different conditions in the two layers. We envisage the overall load in
360 pure granular NaCl samples, at least initially, to have been distributed over “force chains”. The
361 concept of force chains in compacting granular materials considers the overall load to be
362 distributed heterogeneously among the grains, with a minority of grains that carry above-average
363 loads forming a strong load-bearing framework, while the majority of grains constitute a weak

364 granular aggregate (e.g. Peters et al., 2005). In our conceptual model, a force chain will localize
365 pressure solution in a granular NaCl aggregate along an axis that is broadly aligned with the bulk
366 shortening direction and over an initially small grain contact area. The idea of *dynamic force*
367 *chains* entails that the lifetime of a particular force chain is limited by the dynamic redistribution
368 of loads within the granular aggregate as locally increased normal stresses lead to enhanced PSC
369 and accelerated shortening, and a relative increase of the grain surface area along the force
370 chain. When loads are redistributed, the load-bearing framework changes its geometry. Our DVC
371 analysis indicates that the strain within the pure NaCl sample varies in space and time; we
372 interpret this to indicate a rearrangement of stresses and the emergence of new dynamic force
373 chains in the pure NaCl layers.

374 While, in principal, the conceptual model described above may also apply to the NaCl-
375 biotite layer, our DVC analysis indicates that compaction there was tied to the biotite grains and
376 we interpret PSC to have been accelerated by the higher chemical potential associated with
377 phase boundaries (Aharonov and Katsman, 2009; Hickman and Evans, 1995). Factors such as
378 particle shape, particle size, and contact area may also have played a significant role in controlling
379 the evolution of PSC. Meyer et al. (2006) and Van den Ende et al.(2018) demonstrated how
380 particle shapes and the shape of the contact between the particles influence compaction rates
381 in pressure-solution. Pluymakers and Spiers (2015) emphasized the significance of the nature of
382 the contact surfaces where irregularities lead to faster dissolution. The initial geometric
383 arrangement of the grain contacts between a cube and a plate-like mineral (i.e. salt vs biotite)
384 may create ‘asperities’, with lower contact areas, which could have assisted the driving force of
385 the mechanism. From 400 hours onward, the process might have slowed down because reduced

386 porosity was met by reduced asperities/irregularities in the grains, which became progressively
387 smoother as compaction progressed (lower contact stresses). We envisage that these
388 mechanisms contributed to pressure solution. Whichever the reason, the local strain rate data
389 from our DVC analysis suggest that this enhanced PSC drove the initial compaction in the NaCl-
390 biotite layer (Fig. 9). However, with increasing shortening, the contact areas in the NaCl layer
391 increased, which lowered the stresses at contact points and, as a consequence reduced the
392 driving force for PSC. DVC reveals that both the local volumetric and the shear strain rates
393 decreased by almost an order of magnitude in the NaCl-biotite layer between 150 and 400 hours
394 of compaction (Fig. 9, central column), which we consider to be supporting evidence for this
395 interpretation.

396 Compaction of the central NaCl-biotite layer was accompanied by a significant reduction
397 of the porosity, to such a degree that pore connectivity broke down across the central layer early
398 in the experiment (Fig. 3, 4 and 6). However, at the same time, this layer did not compact
399 significantly more than the surrounding NaCl layers (Fig. 5). It is generally assumed that the
400 transport distances during pressure solution of NaCl in a stagnant, saturated brine are on the
401 order of the grain size and material is re-precipitated in the nearby pore space (e.g. Gratier et al.,
402 2013; Gundersen et al., 2002; Weyl, 1959). For our experiments this would mean that the
403 porosity in the NaCl and NaCl-biotite layers should have decreased in proportion with the
404 compaction. Given that this was clearly not the case, porosity reduction in the NaCl-biotite layer
405 cannot have been accomplished by pore collapse during compaction. We speculate that the
406 disproportional decrease of porosity in the NaCl-biotite layer was caused by additional salt being
407 deposited there and, invoke Merino et al.'s model for a texture-pressure solution coupling to

408 explain this (Dewers and Ortoleva, 1988; Merino et al., 1983; Ortoleva et al., 1987). Merino
409 suggests that, in a positive feedback loop, dissolved material should diffuse towards areas with a
410 relatively lower porosity and, therefore, larger grain contact area and correspondingly lower
411 stresses. In our experiment, this would mean that material was transported from the pure NaCl
412 layers to the central NaCl-biotite layer. In the former, the removal of dissolved material leaves
413 less material to carry the load, which increases the driving force for PSC. At the same time, loads
414 are distributed over an increasingly larger area at the deposition sites in the NaCl-biotite layer,
415 which should slow down PSC there. We interpret our quantitative observations to provide
416 evidence that dissolved salt has indeed been transferred from the marginal NaCl into the central
417 NaCl-biotite domain. Once connectivity into the NaCl-biotite was lost, the interface between the
418 two domains would have become the locus for enhanced deposition (Fig. 3).

419 **4.2 Implications for fluid flow and permeability in rocks deforming by PSC**

420 Our experiments provide new insights into the effects of PSC on the spatio-temporal
421 evolution of porosity and pore connectivity, which influence transport properties, and
422 consequently fluid flow. These effects have been intensively studied, particularly for the case of
423 stylolites. Stylolites commonly develop in carbonates, silicate rocks, sandstones and mudstones
424 (Benedicto and Schultz, 2010; Gratier et al., 2013; Heap et al., 2014; Park and Schot, 1968). They
425 can induce up to 50 % of dissolution in the host rock with important implication for solute
426 transport and fluid flow (Aharonov and Katsman, 2009). However, it remains unclear whether
427 stylolites act as barriers to fluid flow (Alsharhan and Sadd, 2010) or become fluid conduits (Heap
428 et al., 2014;). Our experiments, which were conducted under the reported, specific boundary
429 conditions, show that the disconnection of the pore space with increasing deformation leads to

430 a very efficient hydraulic compartmentalization of the sample. The porosity evolution in the
431 central layer would suppress any potential fluid flow across the layer and constrain fluid
432 movements to the NaCl layers, at least at the scale and resolution of our data. At the same time,
433 it would allow fluid that is trapped inside the NaCl-biotite layer to equilibrate chemically with its
434 local host, whereas fluid in the percolating NaCl layers would form part of an open chemical
435 system. Our results support the interpretation by Heap et al. (2014) that stylolites may
436 compartmentalize fluid flow, allowing movement in the marginal layers and in the directions
437 perpendicular to the shortening direction.

438

439 Our findings feed into an improved understanding of fluid transport properties in
440 hydrocarbon reservoirs where PSC is active (Ghanbarzadeh et al., 2015; Torabi et al., 2015).
441 Alsharhan and Sadd (2010) and Heap et al. (2014) show that stylolites are capable of reducing
442 permeability when the rock is enriched in minerals such as phyllosilicates. The effect of biotite
443 on the permeability of the halite rocks remains unclear and will be addressed using a modelling
444 approach in a follow-up study.

445 **5. CONCLUSIONS**

446 We have analysed the first 4D microtomographic dataset that documents pressure
447 solution creep in NaCl-biotite aggregates over several months. Our results indicate that
448 phyllosilicates contribute to reduce bulk porosity and induce a significant decrease in pore
449 connectivity, causing a hydraulic compartmentalization of the sample. The measured local strain
450 rates indicate that phyllosilicates enhance the pressure-solution process by increasing the local
451 strain rates. These results highlight the key role of phyllosilicates in affecting the rock

452 microstructure under pressure-solution creep and provide new insights into the spatio-temporal
453 evolution of transport properties.

454 **ACKNOWLEDGEMENTS**

455 The authors would like to thank Dr. Nicola Cayzer for help at the SEM and Robert Brown and Alex
456 Hart for manufacturing the experimental cells and straining frames. All three are from the School
457 of Geosciences, University of Edinburgh. We furthermore thank Dr. Anne Pluymakers and an
458 anonymous reviewer for extremely encouraging and constructive reviews. The work was
459 supported by the PhD studentship funding from the School of Geosciences, University of
460 Edinburgh.

461 **REFERENCES**

- 462 Aharonov, E., Katsman, R., 2009. Interaction between pressure solution and clays in stylolite
463 development: Insights from modeling. *Am. J. Sci.* 309, 607–632.
464 <https://doi.org/10.2475/07.2009.04>
- 465 Alsharhan, A.S., Sadd, A.L., 2010. Stylolites in Lower Cretaceous Carbonate Reservoirs, U.A.E.
466 *Soc. Sediment. Geol.* <https://doi.org/10.2110/pec.00.69.0185>
- 467 Andò, E., Bésuelle, P., Hall, S.A., Viggiani, G., Desrues, J., 2012. Experimental micromechanics:
468 grain-scale observation of sand deformation. *Géotechnique Lett.* 2, 107–112.
469 <https://doi.org/10.1680/geolett.12.00027>
- 470 Angevine, C.L., Turcotte, D.L., 1983. Porosity reduction by pressure solution: a theoretical
471 model for quartz arenites. *Geol Soc Amer Bull* 94, 1129–1134.
472 [https://doi.org/10.1130/0016-7606\(1983\)94<1129](https://doi.org/10.1130/0016-7606(1983)94<1129)

- 473 Arns, C.H., Knackstedt, M.A., Pinczewski, W. V., Garboczi, E.J., 2002. Computation of linear
474 elastic properties from microtomographic images: Methodology and agreement between
475 theory and experiment. *Geophysics* 67, 1396. <https://doi.org/10.1190/1.1512785>
- 476 Atkinson, M., Bell, A., Curtis, A., Entwistle, E., Filgueira, R., Main, I., Meles, G., Minitier, M., Zhao,
477 Y., 2015. The Terracorrelator : a shared memory HPC facility for real-time seismological
478 cross-correlation analyses. *Geophys. Res. Abstr. Eur. Geosci. Union Gen. Assem.* 17.
- 479 Benedicto, A., Schultz, R.A., 2010. Stylolites in limestone: Magnitude of contractional strain
480 accommodated and scaling relationships. *J. Struct. Geol.* 32, 1250–1256.
481 <https://doi.org/10.1016/j.jsg.2009.04.020>
- 482 Bos, B., Spiers, C.J., 2002. Frictional-viscous flow of phyllosilicate-bearing fault rock :
483 Microphysical model and implications for crustal strength profiles. *J. Geophys. Res.* 107,
484 2028.
- 485 Cnudde, V., Boone, M.N., 2013. High-resolution X-ray computed tomography in geosciences: A
486 review of the current technology and applications. *Earth-Science Rev.* 123, 1–17.
487 <https://doi.org/10.1016/j.earscirev.2013.04.003>
- 488 Croizé, D., Bjørlykke, K., Jahren, J., Renard, F., 2010. Experimental mechanical and chemical
489 compaction of carbonate sand. *J. Geophys. Res. Solid Earth* 115, 1–17.
490 <https://doi.org/10.1029/2010JB007697>
- 491 Dewers, T., Ortoleva, P., 1988. The role of geochemical self-organization in the migration and
492 trapping of hydrocarbons. *Appl. Geochemistry* 3, 287–316. [https://doi.org/10.1016/0883-](https://doi.org/10.1016/0883-2927(88)90108-4)
493 [2927\(88\)90108-4](https://doi.org/10.1016/0883-2927(88)90108-4)
- 494 Dierick, M., Masschaele, B., Hoorebeke, L. Van, 2004. Octopus, a fast and user-friendly

- 495 tomographic reconstruction package developed in LabView®. Meas. Sci. Technol. 15,
 496 1366–1370. <https://doi.org/10.1088/0957-0233/15/7/020>
- 497 Füsseis, F., Schrank, C., Liu, J., Karrech, A., Llana-F??nez, S., Xiao, X., Regenauer-Lieb, K., 2012.
 498 Pore formation during dehydration of a polycrystalline gypsum sample observed and
 499 quantified in a time-series synchrotron X-ray micro-tomography experiment. Solid Earth 3,
 500 71–86. <https://doi.org/10.5194/se-3-71-2012>
- 501 Ghanbarzadeh, S., Hesse, M.A., Prodanović, M., Gardner, J.E., 2015. Deformation-assisted fluid
 502 percolation in rock salt. Science (80-.). 350, 1069–1072.
 503 <https://doi.org/10.1126/science.aac8747>
- 504 Gratier, J.P., 2003. Modeling fluid transfer along California faults when integrating pressure
 505 solution crack sealing and compaction processes. J. Geophys. Res. 108, 1–25.
 506 <https://doi.org/10.1029/2001JB000380>
- 507 Gratier, J.P., 1993. Experimental pressure solution of halite by an indenter technique. Geophys.
 508 Res. Lett. 20, 1647–1650.
- 509 Gratier, J.P., Dysthe, D.K., Renard, F., 2013. The role of pressure solution creep in the ductility of
 510 the Earth ' s upper crust, Advances in Geophysics. <https://doi.org/10.1016/B978-0-12-380940-7.00002-0>
- 511 380940-7.00002-0
- 512 Gratier, J.P., Muquet, L., Hassani, R., Renard, F., 2005. Experimental microstylolites in quartz
 513 and modeled application to natural stylolitic structures. J. Struct. Geol. 1–24.
- 514 Gundersen, E., Renard, F., Dysthe, D.K., Bjørlykke, K., Jamtveit, B., 2002. Coupling between
 515 pressure solution creep and diffusive mass transport in porous rocks. J. Geophys. Res. Solid
 516 Earth 107, ECV 19-1-ECV 19-19. <https://doi.org/10.1029/2001JB000287>

- 517 Heap, M.J., Baud, P., Reuschle, T., Meredith, P.G., 2014. Stylolites in limestones: Barriers to fluid
 518 flow? *Geology* 42, 51–54. <https://doi.org/doi: 10.1130/G34900.1>
- 519 Hickman, S.H., Evans, B., 1995. Kinetics of pressure solution at halite-silica interfaces and
 520 intergranular clay films. *J. Geophys. Res. Earth* 100, 13113–13132.
 521 <https://doi.org/10.1029/95JB00911>
- 522 Hickman, S.H., Evans, B., 1991. Experimental pressure solution in halite : the effect boundary
 523 structure of grain / interphase. *J. Geol. Soc. London.* 148, 549–560.
 524 <https://doi.org/10.1144/gsjgs.148.3.0549>
- 525 Lehner, F., Leroy, Y., 2004. Sandstone Compaction by Intergranular Pressure Solution. Guéguen,
 526 Y., Boutéca, M. (Eds.), *Mech. Fluid-Saturated Rocks. Int. Geophys. Ser. Vol. 89*, pp. 115–168
 527 2004. 1–54.
- 528 Macente, A., Fousseis, F., Menegon, L., Xianghui, X., John, T., 2017. The strain-dependent spatial
 529 evolution of garnet in a high-P ductile shear zone from the Western Gneiss Region
 530 (Norway): a synchrotron X-ray microtomography study. *J. Metamorph. Geol.* 35, 565–583.
 531 <https://doi.org/10.1111/jmg.12245>
- 532 Merino, E., Ortoleva, P., Strickholm, P., 1983. Generation of evenly-spaced pressure-solution
 533 seams during (late) diagenesis: A kinetic theory. *Contrib. to Mineral. Petrol.* 82, 360–370.
 534 <https://doi.org/10.1007/BF00399713>
- 535 Meyer, E.E., Greene, G.W., Alcantar, N.A., Israelachvili, J.N., Boles, J.R., 2006. Experimental
 536 investigation of the dissolution of quartz by a muscovite mica surface: Implications for
 537 pressure solution. *J. Geophys. Res. Solid Earth* 111, 1–4.
 538 <https://doi.org/10.1029/2005JB004010>

- 539 Ortoleva, P., Merino, E., Moore, C., Chadam, J., 1987. Geochemical self-organization I: reaction-
540 transport feedbacks and modeling approach. *Am. J. Sci.*
541 <https://doi.org/10.2475/ajs.287.10.979>
- 542 Park, W.C., Schot, E.H., 1968. Stylolites: their nature and origin. *J. Sediment. Res.* 38, 175–191.
543 <https://doi.org/10.1306/74D71910-2B21-11D7-8648000102C1865D>
- 544 Passchier, C.W., Trouw, R.A.J., 2005. *Microtectonics*.
- 545 Peters, J.F., Muthuswamy, M., Wibowo, J., Tordesillas, A., 2005. Characterization of force chains
546 in granular material. *Phys. Rev. E - Stat. Nonlinear, Soft Matter Phys.* 72, 1–8.
547 <https://doi.org/10.1103/PhysRevE.72.041307>
- 548 Pluymakers, A.M.H., Spiers, C.J., 2015. Compaction creep of simulated anhydrite fault gouge by
549 pressure solution: Theory v. experiments and implications for fault sealing. *Geol. Soc. Spec.*
550 *Publ.* 409, 107–124. <https://doi.org/10.1144/SP409.6>
- 551 Renard, F., Bernard, D., Thibault, X., Boller, E., 2004. Synchrotron 3D microtomography of halite
552 aggregates during experimental pressure solution creep and evolution of the permeability.
553 *Geophys. Res. Lett.* 31, 1–4. <https://doi.org/10.1029/2004GL019605>
- 554 Renard, F., Dysthe, D., Feder, J., Bjorlykke, K., Jamtveit, B., 2001. Enhanced pressure solution
555 creep rates induced by clay particles: Experimental evidence in salt aggregates. *Geophys.*
556 *Res. Lett.* 28, 1295–1298. <https://doi.org/10.1029/2000GL012394>
- 557 Renard, F., Ortoleva, P., Gratier, J.P., 1997. Pressure solution in sandstones: influence of clays
558 and dependence on temperature and stress. *Tectonophysics* 280, 257–266.
559 [https://doi.org/10.1016/S0040-1951\(97\)00039-5](https://doi.org/10.1016/S0040-1951(97)00039-5)
- 560 Rutter, E.H., 1983. Pressure solution in nature, theory and experiment. *J. Geol. Soc. London*.

- 561 140, 725–740. <https://doi.org/10.1144/gsjgs.140.5.0725>
- 562 Rutter, E.H., Wanten, P.H., 2000. Experimental Study of the Compaction of Phyllosilicate-
563 Bearing Sand at Elevated Temperature and with Controlled Pore Water Pressure. *J.*
564 *Sediment. Res.* 70, 107–116. [https://doi.org/10.1306/2DC40902-0E47-11D7-](https://doi.org/10.1306/2DC40902-0E47-11D7-8643000102C1865D)
565 [8643000102C1865D](https://doi.org/10.1306/2DC40902-0E47-11D7-8643000102C1865D)
- 566 Schindelin, J., Arganda-Carreras, I., Frise, E., Kaynig, V., Longair, M., Pietzsch, T., Preibisch, S.,
567 Rueden, C., Saalfeld, S., Schmid, B., Tinevez, J.-Y., White, D.J., Hartenstein, V., Eliceiri, K.,
568 Tomancak, P., Cardona, A., 2012. Fiji: an open-source platform for biological-image
569 analysis. *Nat. Methods* 9, 676–682. <https://doi.org/10.1038/nmeth.2019>
- 570 Schutjens, P.M.T.M., Spiers, C.J., 1999. Intergranular pressure solution in NaCl: Grain-to-grain
571 contact experiments under the optical microscope. *Oil Gas Sci. Technol.* 54, 729–750.
572 <https://doi.org/10.2516/ogst:1999062>
- 573 Spiers, C.J., Schutjens, P.M.T.M., Brzesowsky, R.H., Peach, C.J., Liezenberg, J.L., Zwart, H.J.,
574 1990. Experimental determination of constitutive parameters governing creep of rocksalt
575 by pressure solution. *Geol. Soc. London, Spec. Publ.* 54, 215–227.
576 <https://doi.org/10.1144/GSL.SP.1990.054.01.21>
- 577 Sprunt, E.S., Nur, A., 1977. Destruction of porosity through pressure solution. *Geophysics* 42,
578 726–741.
- 579 Sprunt, E.S., Nur, A., 1976. Reduction of porosity by pressure solution: Experimental
580 verification. *Geology* 4, 463–466.
- 581 Torabi, A., R.H., G., Fossen, H., Pingrose, P., Skurtveit, E., Ando', E., 2015. Strain localization in
582 sandstone and its implications for CO₂ storage. *First Break* 33, 81–92.

583 Tudisco, E., Andò, E., Cailletaud, R., Hall, S.A., 2017. TomoWarp2: A local digital volume
584 correlation code. *SoftwareX* 6, 267–270. <https://doi.org/10.1016/j.softx.2017.10.002>

585 Van den Ende, M.P.A., Marketos, G., Niemeijer, A.R., Spiers, C.J., 2018. Investigating
586 Compaction by Intergranular Pressure Solution Using the Discrete Element Method. *J.*
587 *Geophys. Res. Solid Earth*. <https://doi.org/10.1002/2017JB014440>

588 Weyl, P.K., 1959. Pressure solution and the force of crystallization: a phenomenological theory.
589 *J. Geophys. Res.* 64, 2001–2025. <https://doi.org/10.1029/JZ064i011p02001>

590 **FIGURE CAPTIONS**

591 **Figure 1** a) Horizontal XY μ CT slice and b) vertical XZ μ CT slice of the NaCl-biotite sample, showing
592 the different attenuation values of the materials: biotite in bright colour, NaCl grains in light grey
593 and (brine-filled) pores in dark grey.

594 **Figure 2** a) Compaction curves for the two samples (top). Roman numbers indicated the number
595 of the 12 μ CT dataset acquired: the reference scan is not numbered (see section 3.2). b) Evolution
596 of bulk strain rates with increasing deformation for the two samples, in log-log scale.

597 **Figure 3** Vertical μ CT slices of four different shortened datasets, for pure NaCl (left column) and
598 NaCl-biotite samples (right column), respectively. Roman numbering refers to Figure 2a. White
599 arrows indicate areas of reduced porosity, where NaCl grains indent more, losing their cubic
600 habit, and/or precipitation sites.

601 **Figure 4** a) Evolution of the pore volume (in μm^3) in the two sample compositions for increasing
602 compaction time (hours). The percentages inside the bars indicate the porosity, calculated
603 through the *Volume Fraction* operator from the 400^3 voxels subvolumes (see section 2.2.4). Initial
604 porosity fraction (ϕ_0), calculated from the undeformed 400^3 voxels subvolumes, is given in the

605 legend for the two samples. Errors bars obtained through erosion and dilation of original
606 segmented pore space. b, c, d) Temporal evolution (in hours, 'hs') of porosity slice by slice
607 ("Porosity 2D") as a function of the vertical Z axis for the two samples.

608 **Figure 5** Relative shortening of the biotite-bearing and NaCl-bearing layers. The grey shaded area
609 indicates the time interval over which pore connectivity breaks down within the NaCl-biotite
610 layer (see section 3.2.2).

611 **Figure 6** Interconnectivity of the pore space as a function of deformation for the two samples.
612 Different colours indicate disconnected pore clusters.

613 **Figure 7** DVC results for the NaCl sample, for increasing compaction time (indicated in hours, 'hs')
614 and vertical shortening (in percentage). Images are obtained as vertical slices through the middle
615 of the sample. For a better comparison, maximum shear strain (*Shear Strain*) and volumetric
616 strain (*Volum. Strain*) results are reported together with the pair of *x-ray* μ CT images used for the
617 correlation for each interval time. Black areas identify locations where the correlation failed.
618 Higher values of maximum shear strain are represented in the images by warmer colours, while
619 negative values of volumetric strain (indicating compaction) are represented by blue colours
620 (white circles). Note the relatively homogeneous distribution of shear strains, with local highs.

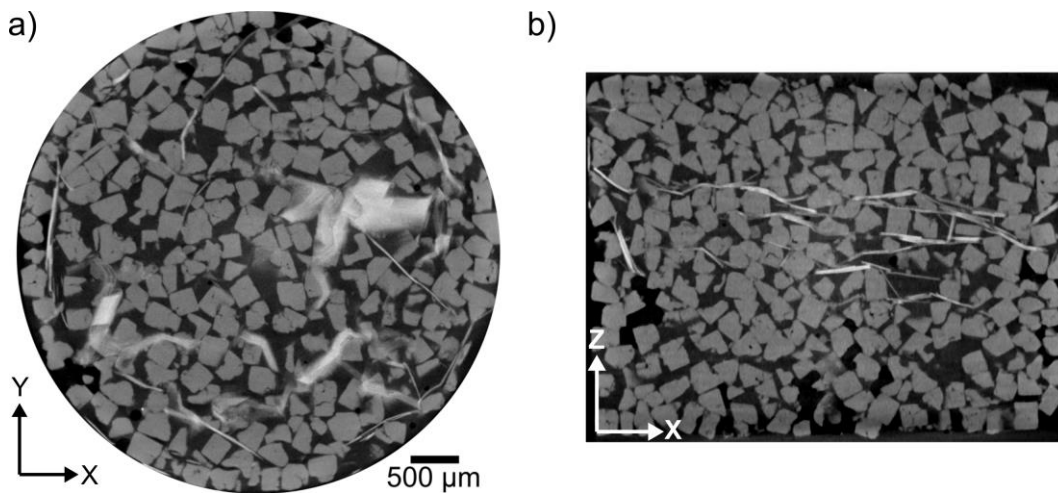
621 **Figure 8** DVC results for the NaCl-biotite sample, for increasing compaction time (indicated in
622 hours, 'hs') and vertical shortening (in percentage). Images are obtained as vertical slices through
623 the middle of the sample. For a better comparison, maximum shear strain (*Shear Strain*) and
624 volumetric strain (*Volum. Strain*) results are reported together with the pair of *x-ray* μ CT images
625 used for the correlation for each interval time. Black areas identify locations where the
626 correlation failed. Higher values of maximum shear strain are represented in the images by

627 warmer colours, while negative values of volumetric strain (indicating compaction) are
 628 represented by blue colours (white circles). Note the extreme intense values in areas where the
 629 biotite flakes are located (high shear strains, negative volumetric strains).

630 **Figure 9** The images show the distributions of local strain rates (in s^{-1}), calculated from DVC
 631 results, for both samples: a) maximum shear strain rates, b) volumetric strain rates. To obtain the
 632 strain rates, the strain values, obtained from the DVC results, are divided by the time interval
 633 between each pair of correlations. Black areas identify locations where the correlation failed.

634 **Figure 10** SEM images of recovered samples: a) triple junction (highlighted by white arrows)
 635 between grains in the pure NaCl sample; b) close up from the red square in a, note the suture
 636 zone (white arrows) between NaCl grains; c, d) NaCl grains indenting biotite flakes (Bt) in the
 637 NaCl-biotite sample.

638



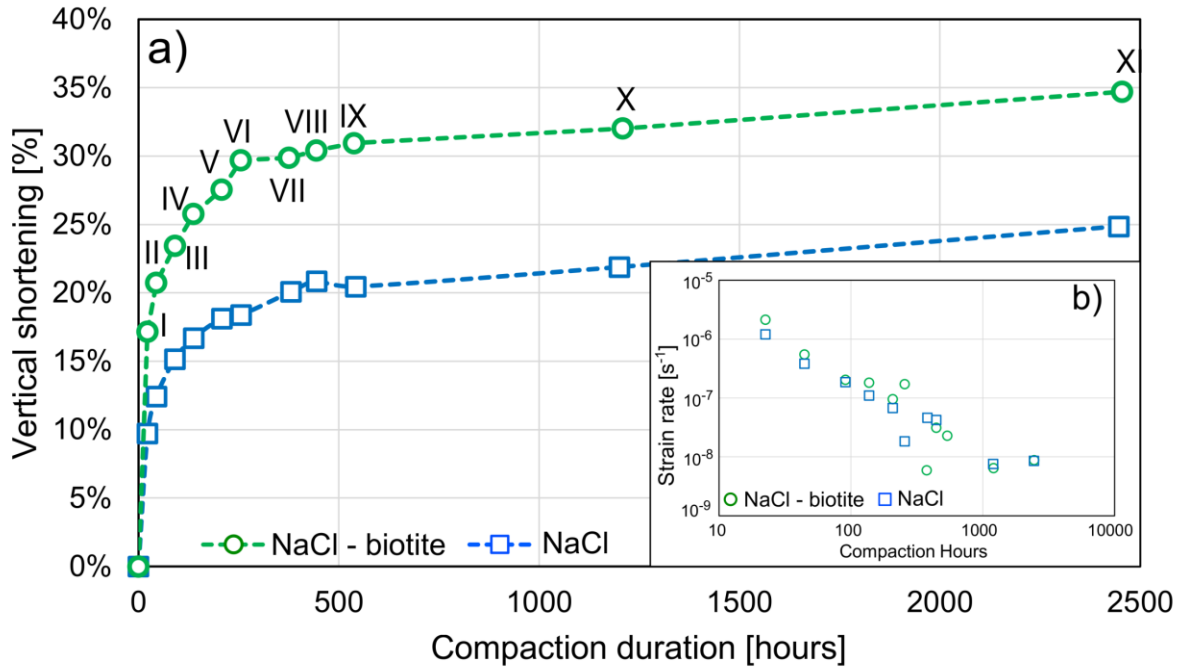
639

640

641

642

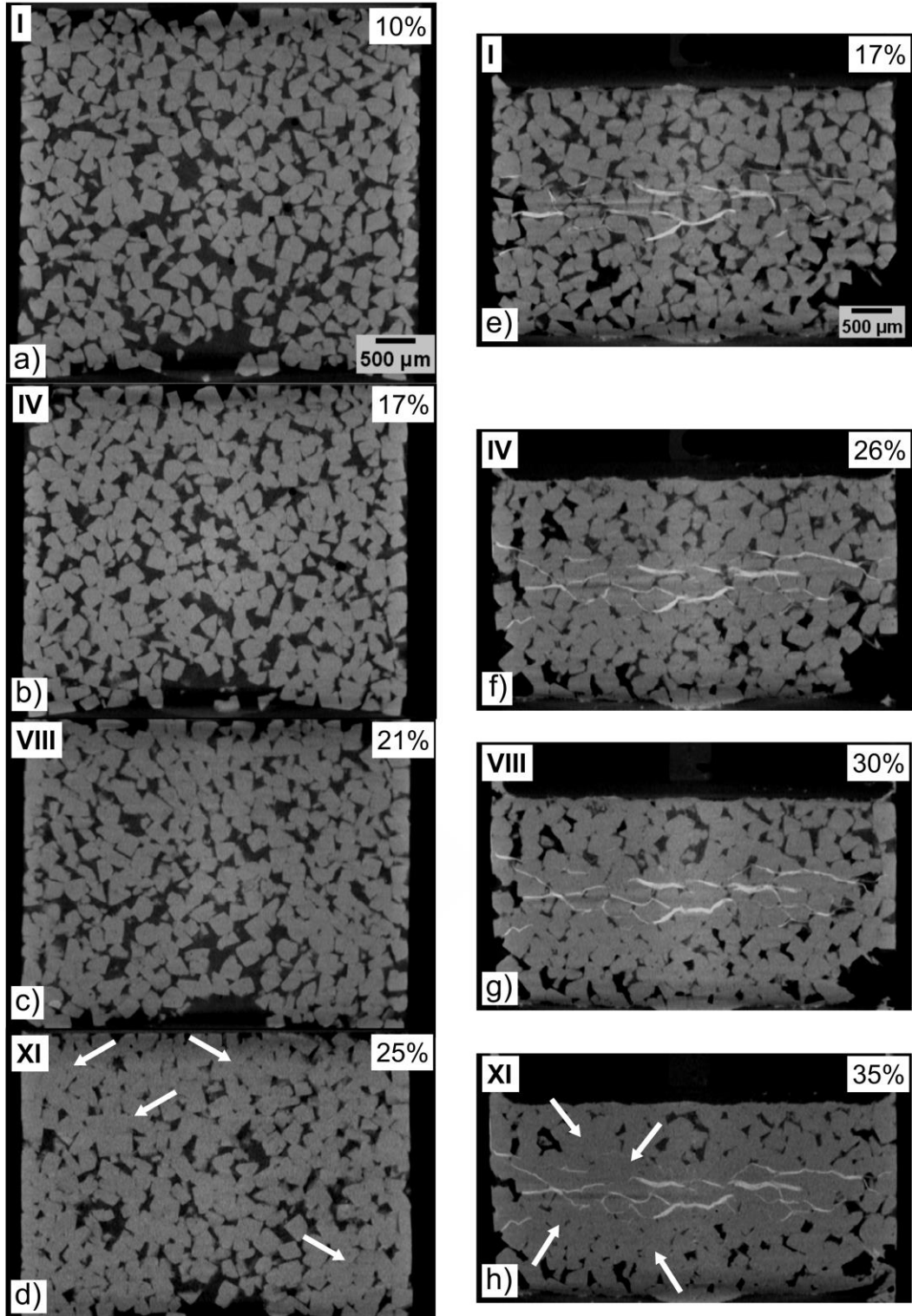
Figure 1



643

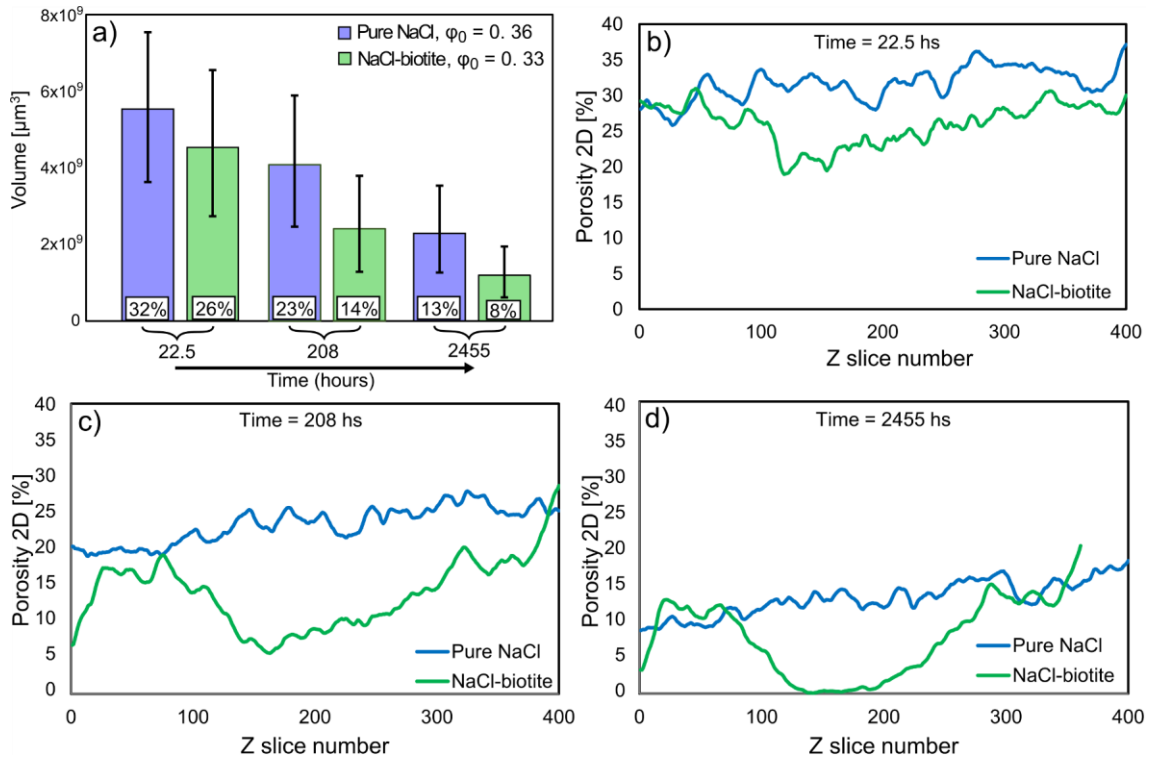
644

Figure 2



645
646

Figure 3

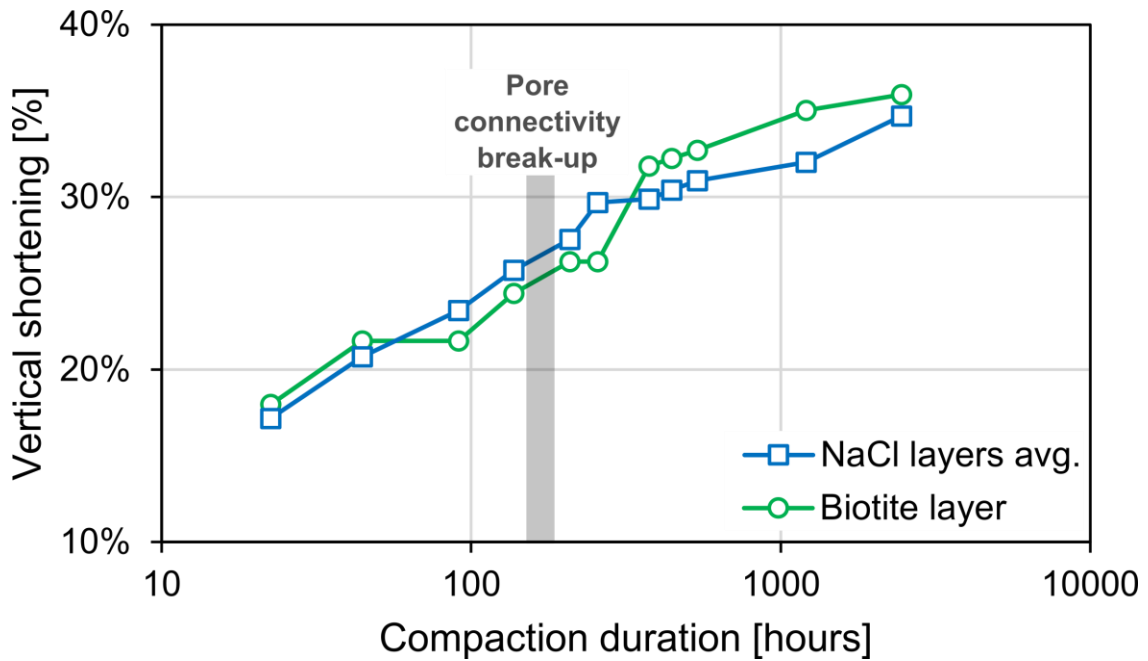


647

648

649

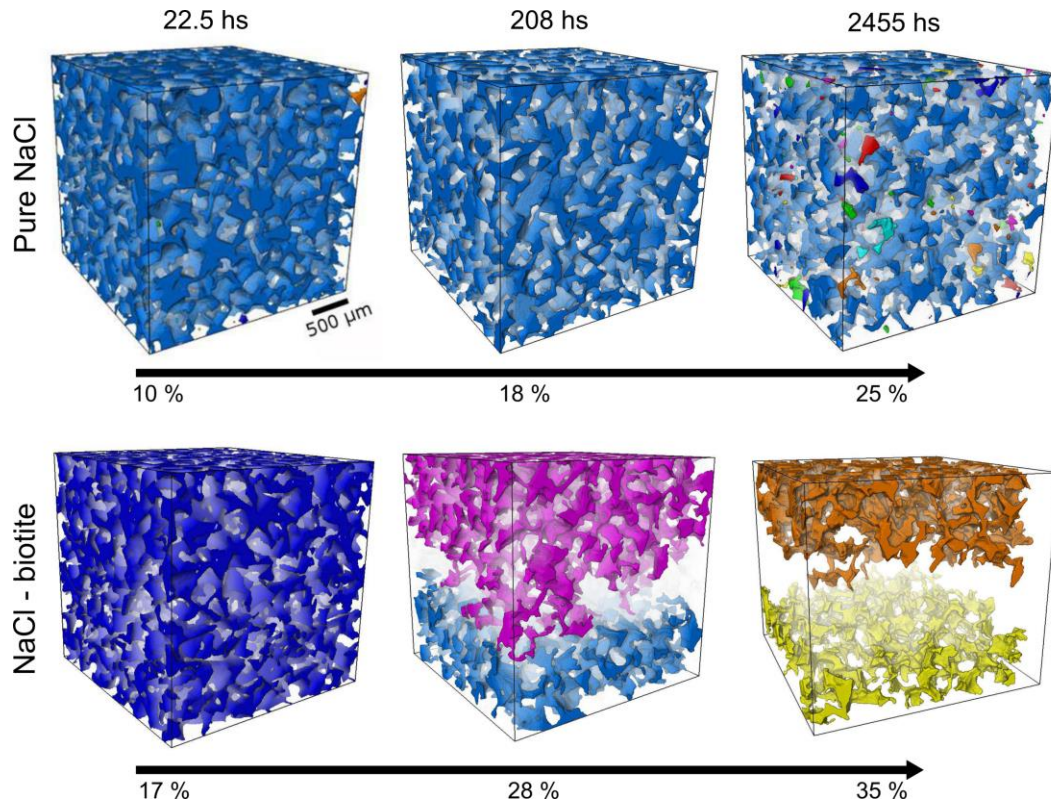
Figure 4



650

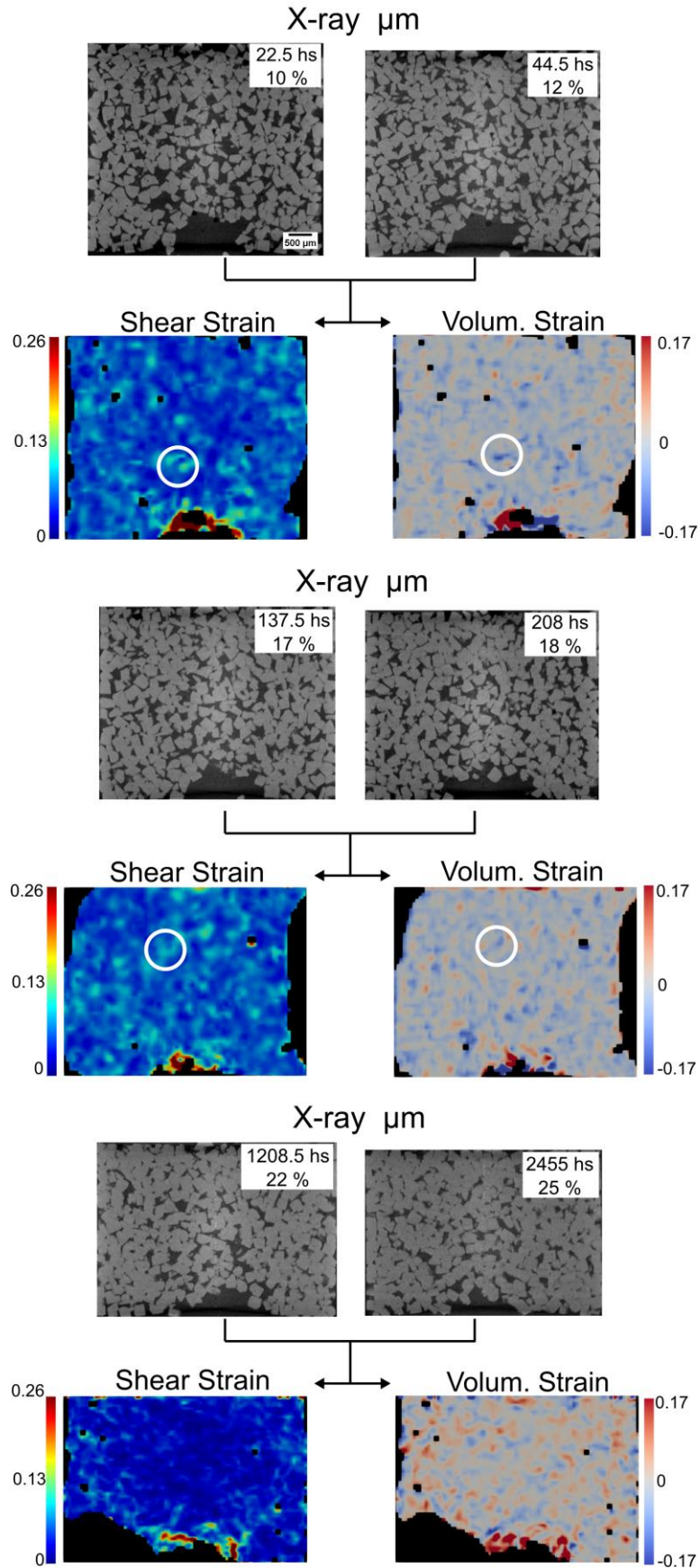
651

Figure 5



652
653
654

Figure 6



656

Figure 7

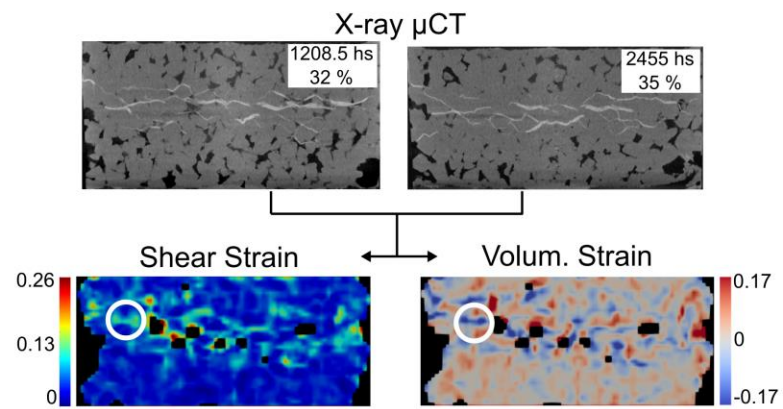
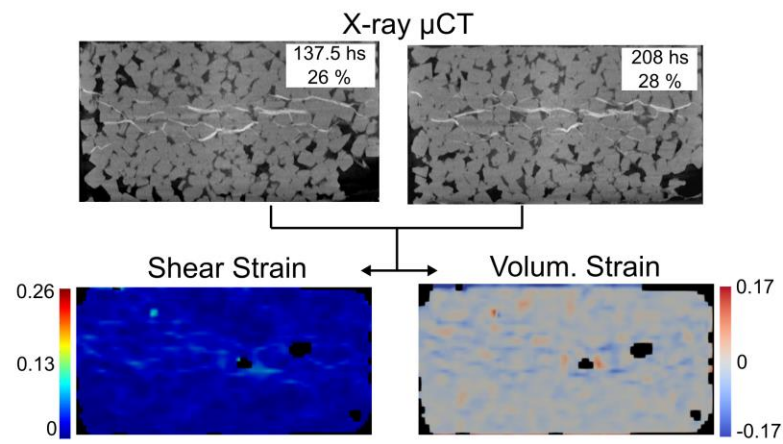
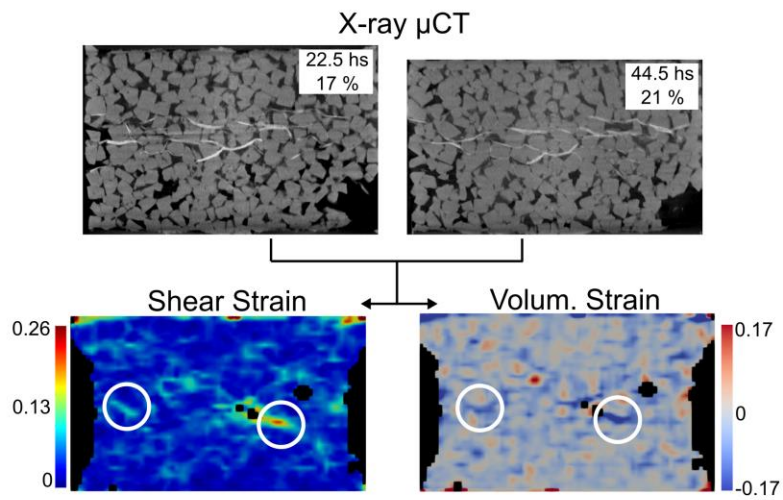


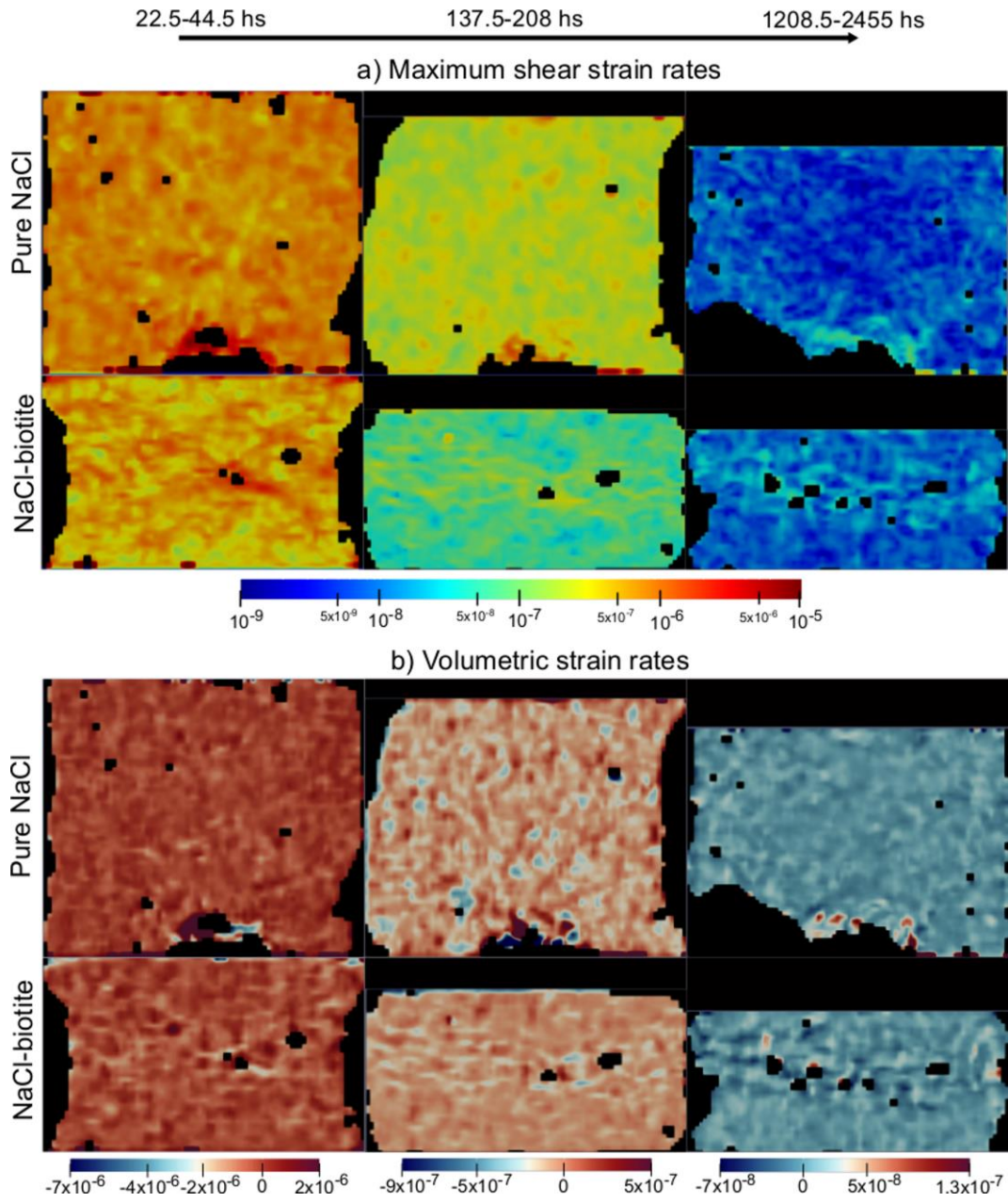
Figure 8

657

658

659

660



661

662

Figure 9

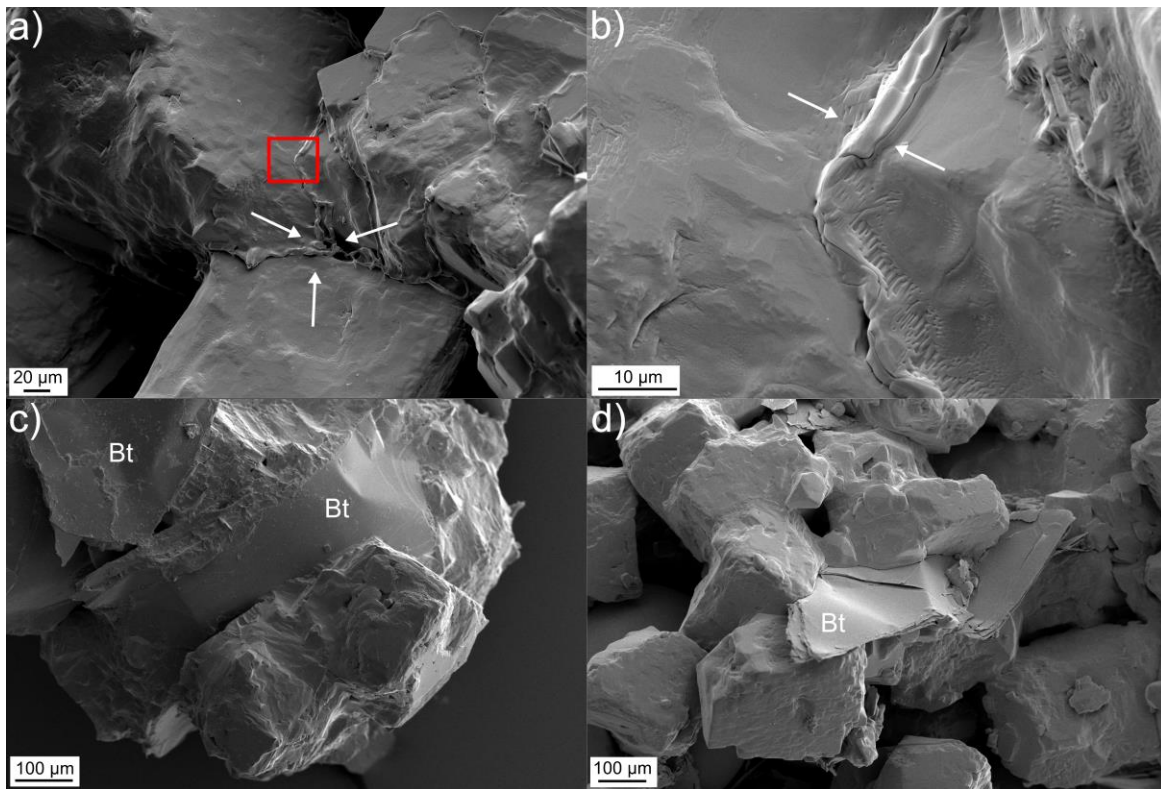


Figure 10

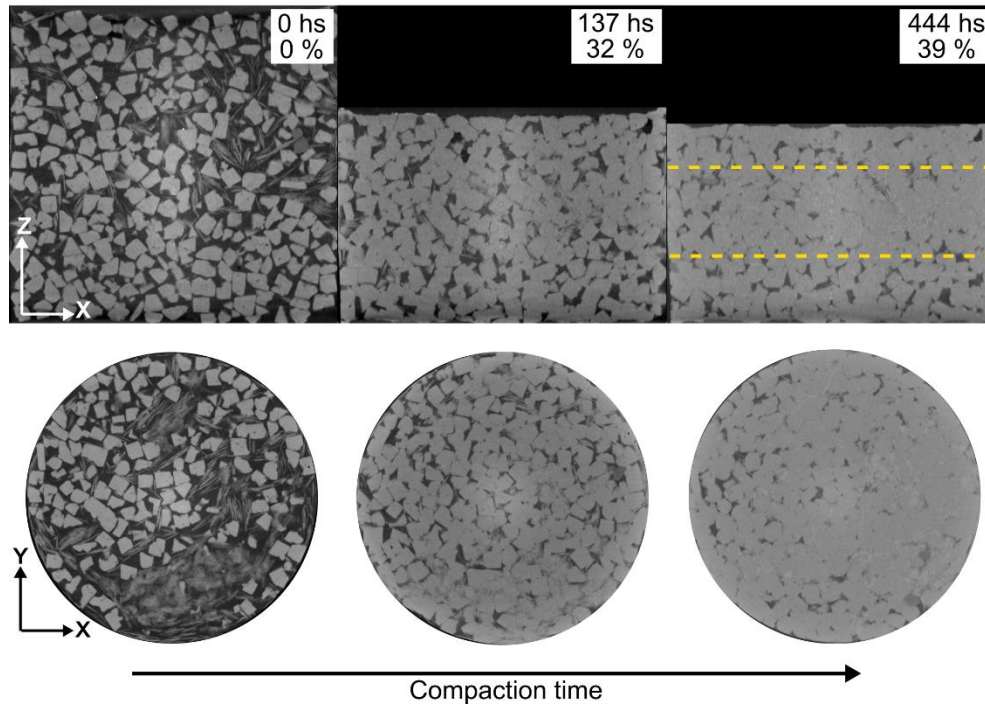
663
664
665

SUPPLEMENTARY MATERIAL

667

Additional NaCl-biotite experiment

668
669 A previous shorter experiment of mixture of NaCl and biotite was conducted. In that experiment,
670 biotite grains were sieved to 180-212 µm and they were not pre-localised in the centre of the
671 sample (Fig. S1). The sample compacted for 444 hours, with a load of 6.6 MPa. Over time, the
672 sample showed a localised reduction in bulk porosity and pore connectivity nearby biotite flakes,
673 however, to a lower degree than the data presented here. It also showed a progressive
674 concentration of the biotite grains towards the centre of the sample, a similar behaviour to the
675 study presented. However, individual biotite flakes are not recognizable anymore.



676

677 **Figure S1** μ CT slices showing the evolution of the microstructure for a previous experiment compacting a
 678 mixture of NaCl and biotite grains. The biotite was sieved between 180-212 μm and was not pre-localised
 679 (long flakes). Compaction time is shown in hours (abbr. 'hs'), and vertical shortening as percentage.
 680 Sample width is 5mm. Top: Vertical XZ μ CT slices, cut from the middle of the sample; bottom) XY slices,
 681 half height of the sample. With increasing compaction, the biotite grains are not distinguishable anymore.
 682 However, a central volume of reduced porosity is recognizable at the end of the experiment (yellow
 683 dashed lines).
 684

684

685 **Fundamentals of Digital Volume Correlation (DVC)**

686 Digital Image Correlation (DIC) is a correlation analysis technique, which measures
 687 displacements, maximum shear and volumetric strains of planar and non-planar surfaces
 688 undergoing deformation (Hall et al., 2009; Lenoir et al., 2007). In recent years, this technique has
 689 been extensively used in experimental geomechanics and in solid and fluid mechanics to obtain
 690 *full field kinematics* and *strain field* analysis. It has recently increased in popularity, thanks also
 691 to the development of non-destructive image techniques, such as X-ray microtomography, where
 692 3D volumes obtained by X-ray microtomography are correlated together to identify internal
 693 deformation of the samples and quantify the strains (Digital Volume Correlation, DVC) (Hall,
 694 2012; Hall et al., 2009; Lenoir et al., 2007). DVC can also be used to identify and track the
 695 evolution of internal structures of the sample, that is otherwise invisible in the X-ray data, or to
 696 quantify porosity evolution in the rock. We used DVC on increasingly shortened μ CT data.

697 The steps that DIC (and DVC) performs on the images (or volumes) involve (Fig. S2):

- 698 1. Definition of *nodes* distributed over the "reference image" (Fig. S2, step 1);
- 699 2. Definition of the *correlation window*, which defines the region centred in each node. The initial
700 integer positions in the reference image are defined by the positions of four manually selected
701 vertices. Only nodes within this subset will be analysed. The nodes are chosen semi-automatically
702 on the basis on the grey values in the correlation window, and on the appropriate threshold. This
703 defines the correlation window.
- 704 3. Calculation of the correlation coefficient for each displacement of the correlation window
705 within an area (*search window*) around the target node of the second image;
- 706 4. Definition of the actual displacements (*discrete displacement*) (Fig. S2, step 2).
- 707 5. Sub-pixel refinement and calculation of *full 3D strain tensor field* from which the maximum
708 shear and volumetric strains are calculated (Hall et al., 2009; Lenoir et al., 2007) (Fig. S2, steps 3-
709 4).

710

711 The strain invariants are calculated from the 3D strain tensor fields according to the following
712 equations. Volumetric strains are calculated through:

713

$$714 \quad \varepsilon_v = \varepsilon_1 + \varepsilon_2 + \varepsilon_3$$

715

716 while the maximum shear strains:

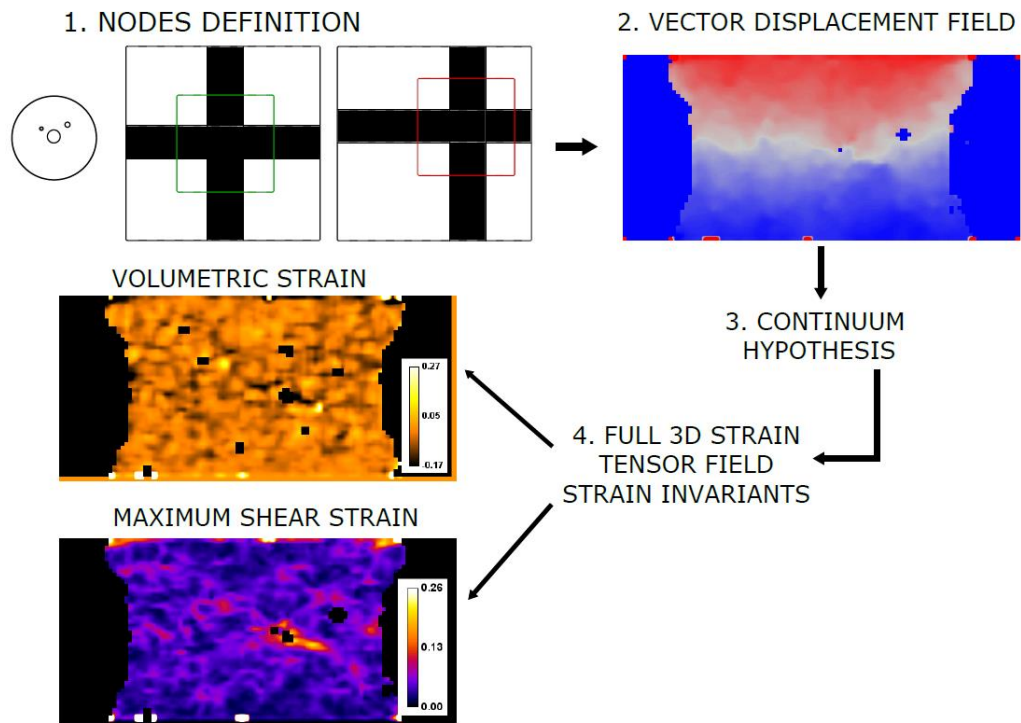
717

$$718 \quad \varepsilon_s = \sqrt{\left(\frac{\varepsilon_1 - \varepsilon_2}{2}\right)^2 + \left(\frac{\varepsilon_1 - \varepsilon_3}{2}\right)^2 + \left(\frac{\varepsilon_2 - \varepsilon_3}{2}\right)^2}$$

719

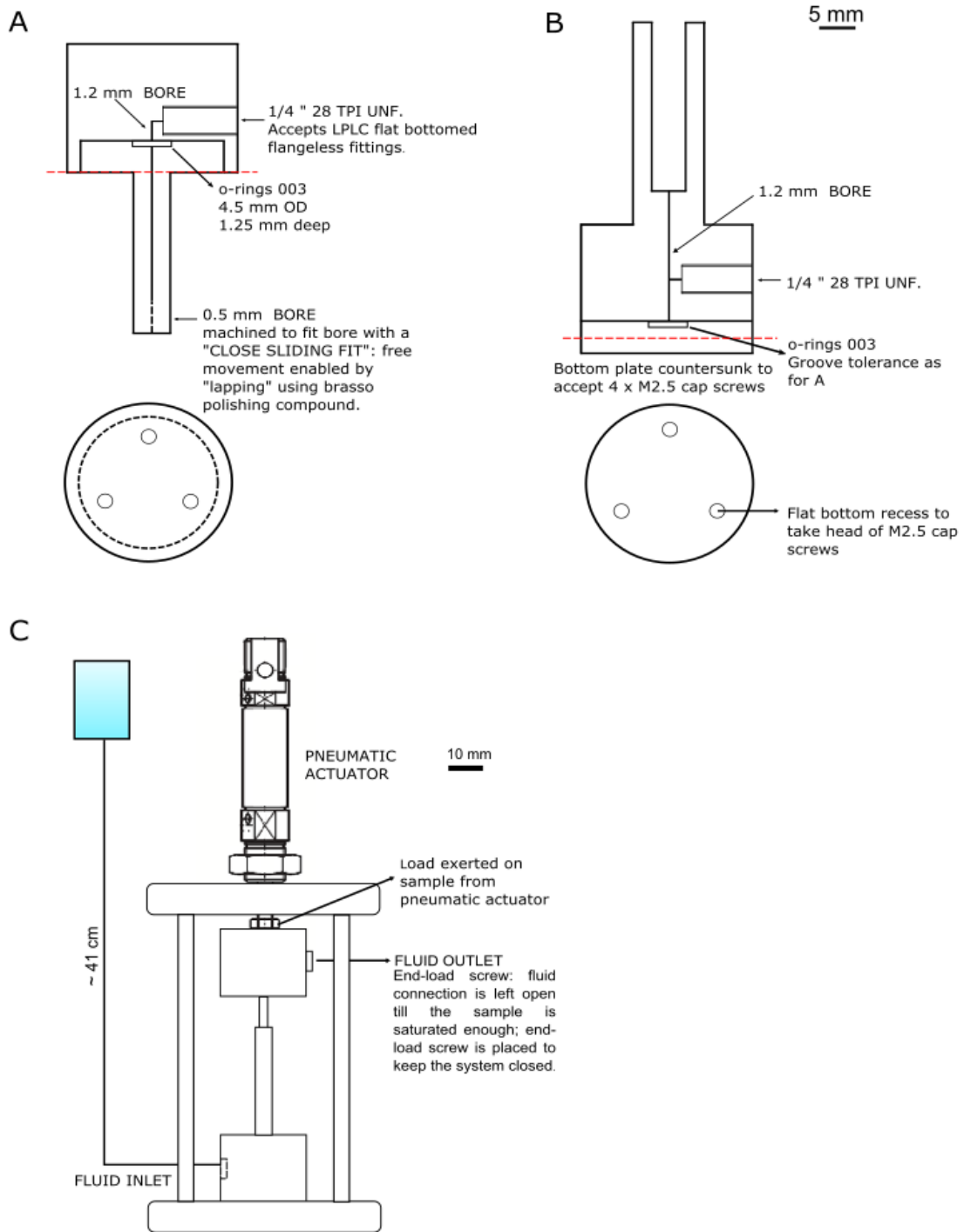
720 The *subset overlap*, which is the overlap given by the node spacing and the correlation window
721 size, defines the resolution and the smoothing of the results. If the correlation window is too
722 large or too small, this will lead to poor correlation (percentages values < 99%) and/or very noisy
723 results. The same is true for the search window size and node spacing. Uncorrelated areas will
724 be left blank (black colour) in the outputs. Furthermore, the code allows to set up a post-
725 processing filter to smooth the outputs.

726



727

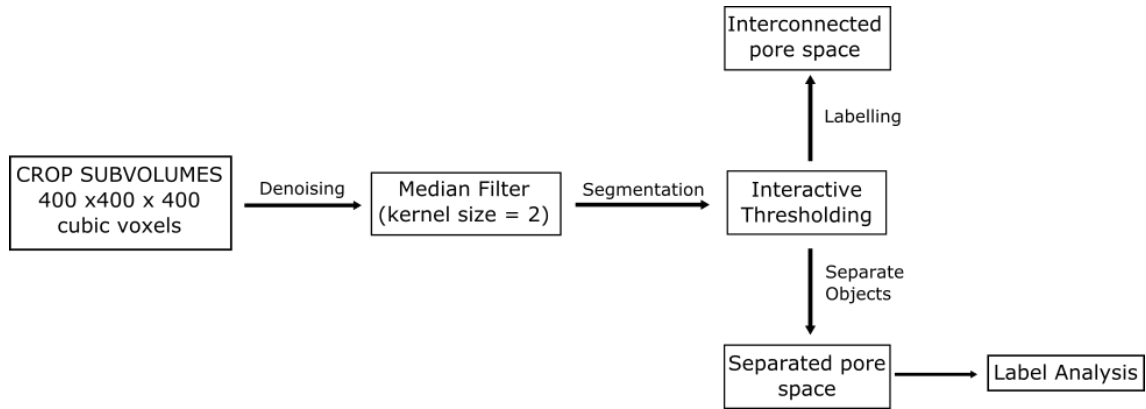
728 **Figure S2** Explanation of the steps operated by DVC in order to get full displacements fields, and the strain
 729 invariants. After definition of a correlation window (green) and a search window (red), the vector
 730 displacement field is calculated. From this, through a continuum hypothesis, the full 3D strain tensor field
 731 is calculated, and therefore the maximum shear and volumetric strains values. The images refer to the
 732 outputs for the sample NaCl-biotite, after 44.5 hours compaction and 21 % vertical shortening.



733

734 **Figure S3** Illustration showing the different components of the experimental setup: A) Top piston and
 735 cross-sectional view (red dashed line); B) Lower chamber and cross-sectional view of the base (red dashed
 736 line); C) Schematic sketch illustrating the position of the sample vessel, within the frame, the position of
 737 the pneumatic actuator, and the fluid reservoir. Pneumatic actuator, 25 mm bore. Scale in figures.

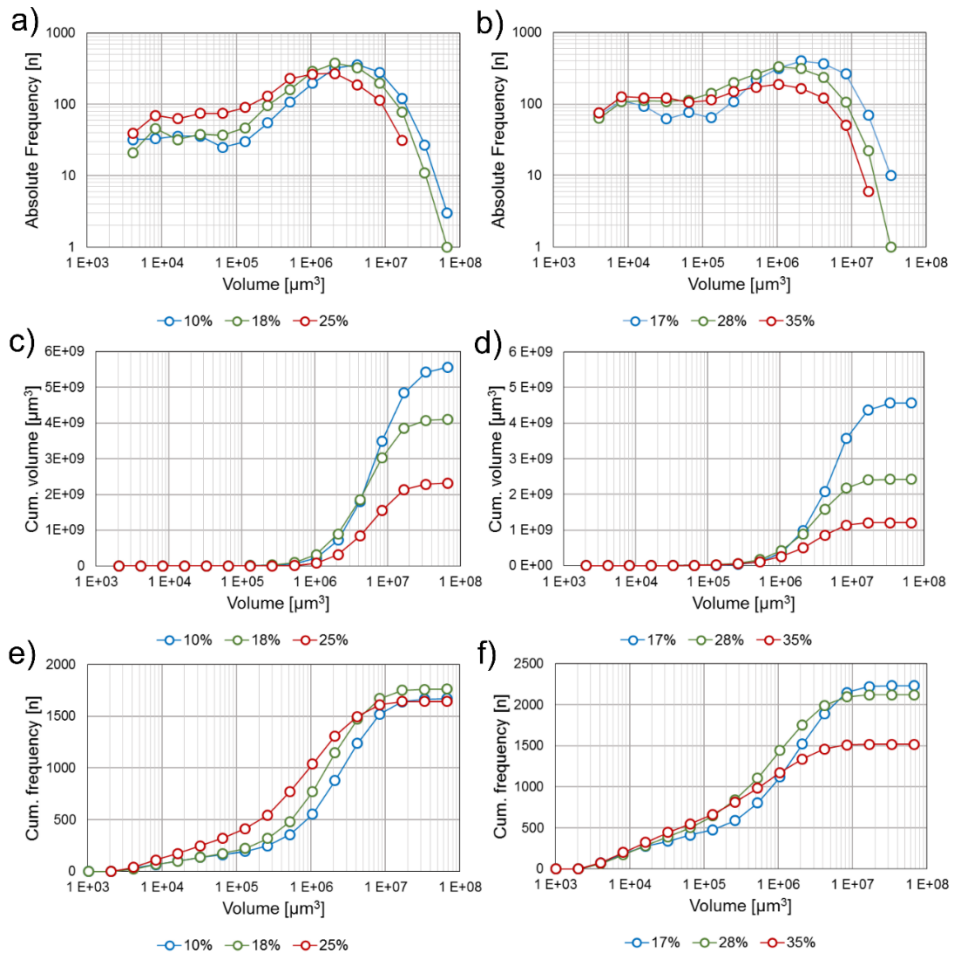
738



739

740

741 **Figure S4** Schematic illustration to explain the workflow used to analyse the pore space.



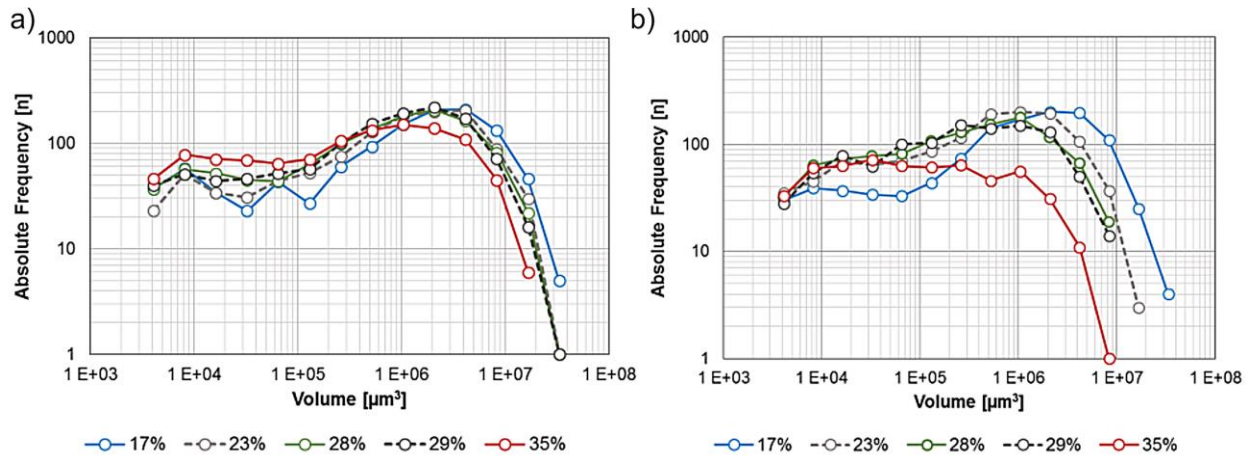
742

743 **Figure S5** a) Absolute Frequency pure NaCl sample. b) Absolute Frequency NaCl-biotite sample. c, e)

744 Cumulative volume and cumulative frequency, respectively, of pure NaCl sample. d, f) Cumulative volume

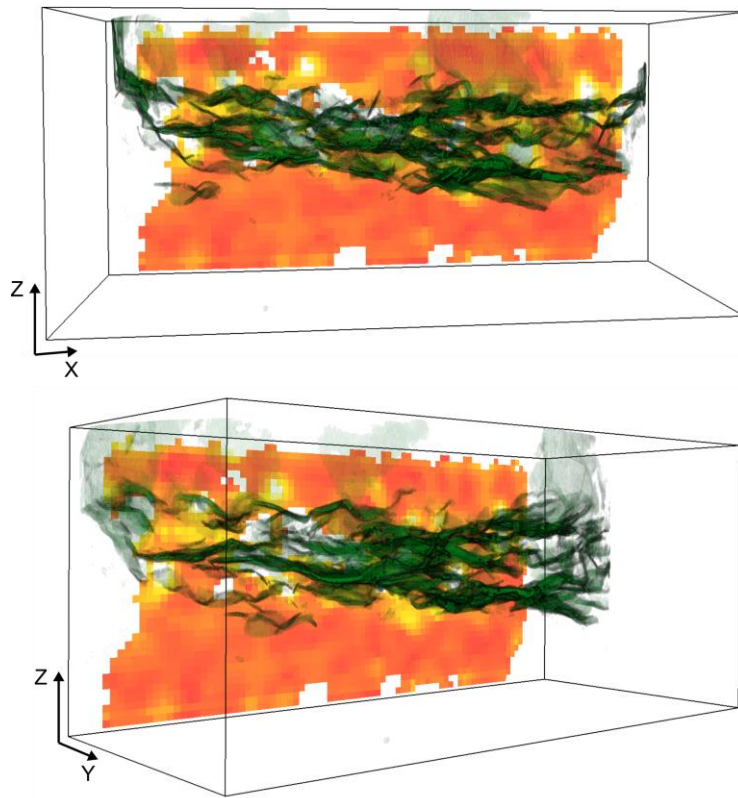
745 and cumulative frequency of NaCl-biotite sample.

746



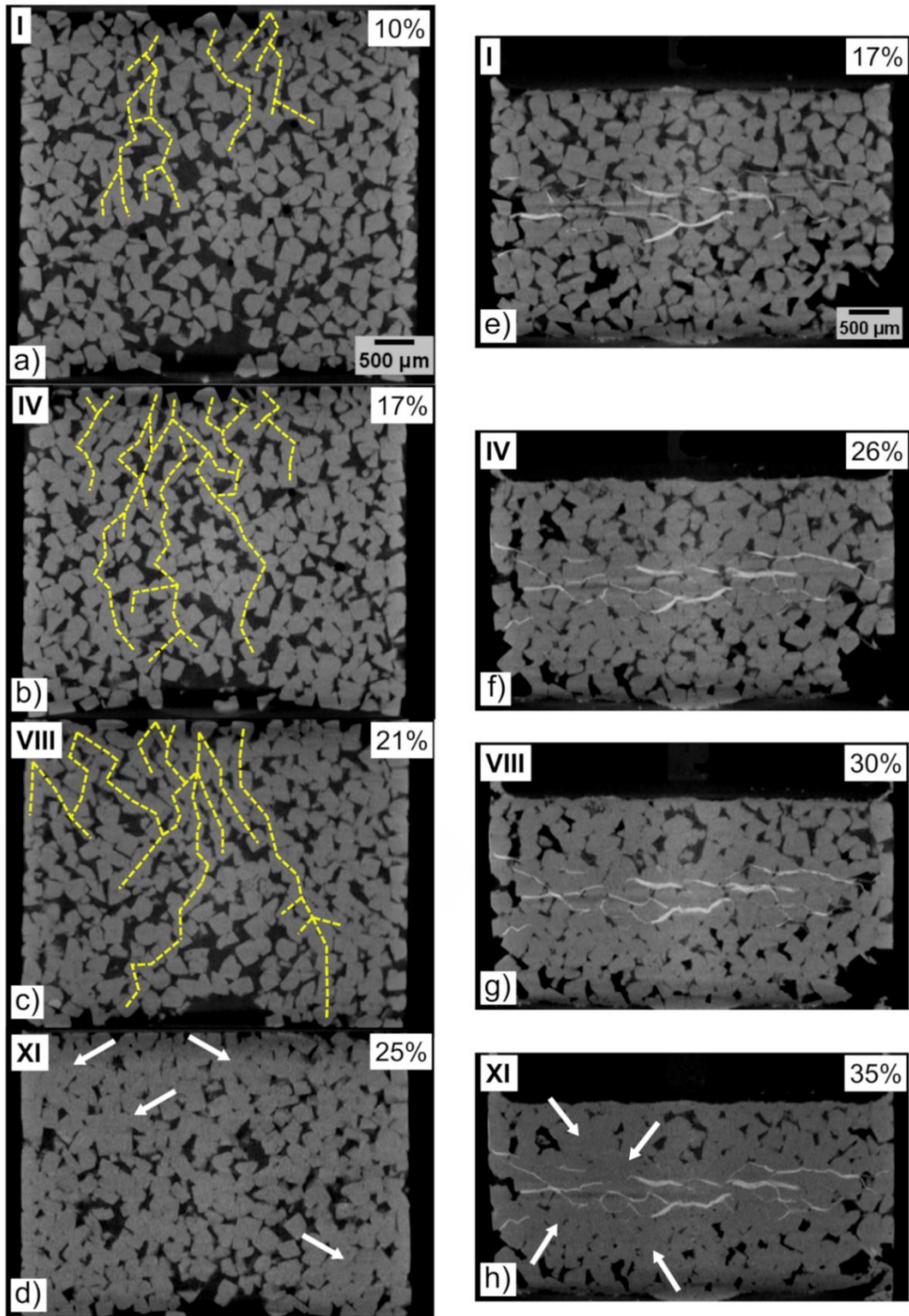
747
748
749

Figure S6 Pore size distributions plots for NaCl-Biotite sample: A) NaCl layers, B) Biotite layer.



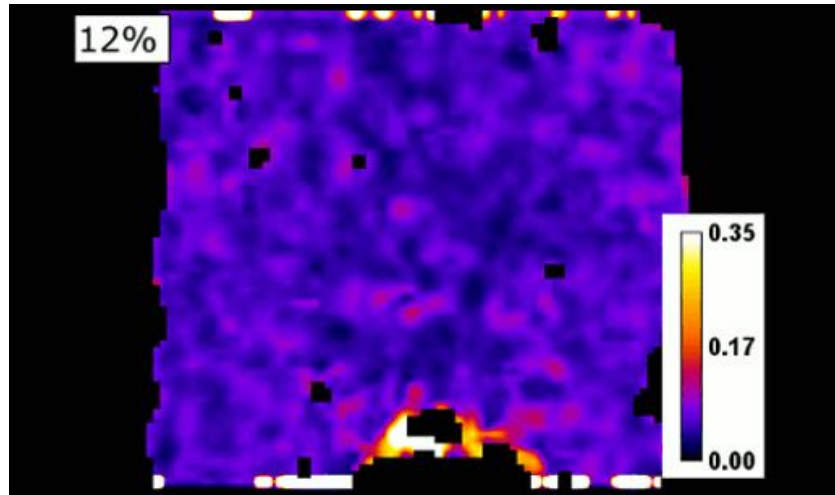
750
751
752
753
754

Figure S7 3D volume rendering of biotite flakes at the end of experiment, and vertical slices of the maximum shear strain derived from DVC: the highest values (yellow colour) are located where the biotite flakes are present.



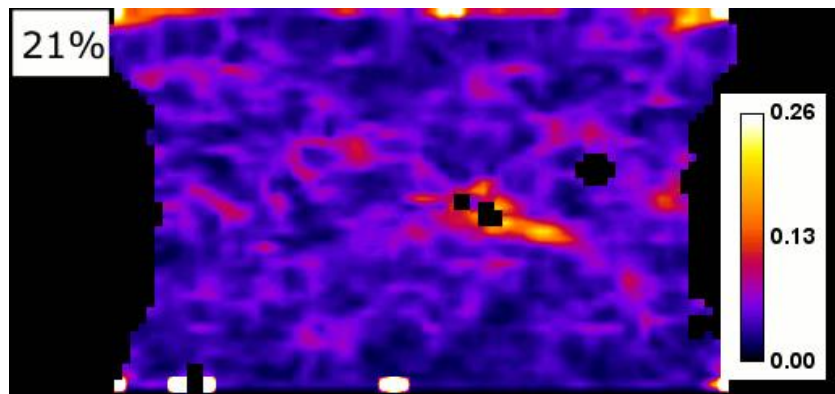
755
756
757
758

Figure S8 The yellow traced lines estimate the location of *dynamic force chains*, on top of Fig. 3.



759
760
761
762
763

Gif 1 Time-dependent evolution of maximum shear strains in the pure NaCl sample. Vertical shortening indicated as percentage on top left. Warmer colours indicate higher maximum shear strains.



764
765
766
767
768

Gif 2 Time-dependent evolution of maximum shear strains in the NaCl-biotite sample. Vertical shortening indicated as percentage on top left. Darker colours indicate negative volumetric strains, and they represent compaction fields.

769 **Table S1** Summary of the CT working conditions for the experiments. An aluminium filter was used to
770 prevent the most compacted datasets for beam hardening artefacts.

Target Power	70 kV
Projections	2000
Exposure Time (s)	2
Energy Filter	Al (0.8 mm thick)
Reconstructed voxel size (μm)	6.5
Mass (g) per sample:	0.13 g (<i>Pure NaCl sample</i>)
	0.10 g NaCl 0.02 g Bt (20% mass) (<i>NaCl+Bt sample</i>)

771 **Table S2** Table indicating the time at which each scan was taken, and the relative vertical shortening
 772 measured.
 773

Scan N°	Pure NaCl sample		NaCl+biotite sample	
	Compaction time (hours)	Vertical Shortening (%)	Compaction time (hours)	Vertical Shortening (%)
0	0	0	0	0
I	22,5	10	22,5	17
II	44,5	12	44,5	21
III	91	15	91	23
IV	137,5	17	137,5	26
V	208	18	208	28
VI	256	18	256	30
VII	380,5	20	376	30
VIII	444,5	21	444,5	30
IX	542	20	538,5	31
X	1200	22	1208,5	32
XI	2446,5	25	2455	35

774

775 **SUPPLEMENTAL REFERENCE LIST**

776 Hall, S.A., 2012. Digital Image Correlation in Experimental Geomechanics. ALERT Dr. Sch. Exp.
 777 Tech. Geomech.

778 Hall, S.A., Muir Wood, D., Ibraim, E., Viggiani, G., 2009. Localised deformation patterning in 2D
 779 granular materials revealed by digital image correlation. Granul. Matter 12, 1–14.

780 <https://doi.org/10.1007/s10035-009-0155-1>

781 Lenoir, N., Bornert, M., Desrues, J., Bésuelle, P., Viggiani, G., 2007. Volumetric digital image
 782 correlation applied to x-ray microtomography images from triaxial compression tests on
 783 argillaceous rock. Strain 43, 193–205. <https://doi.org/10.1111/j.1475-1305.2007.00348.x>

784

785